Spatio-temporal Snow Variability in a Sub-Alpine Forest predicted by Machine Learning and UAV-based LiDAR Snow Depth Maps

Joschka Geissler[1], Lars Rathmann[1], and Markus Weiler[1]

[1]University of Freiburg, Germany

January 24, 2023

Abstract

Snow interacts with its environment in many ways, is constantly changing with time, and thus has a highly heterogeneous spatial and temporal variability. Therefore, modeling snow variability is difficult, especially when additional components such as vegetation add complexity. To increase our understanding of the spatio-temporal variability of snow and to validate snow models, we need reliable observation data at similar spatial and temporal scales. For these purposes, airborne LiDAR surveys or time series derived from snow sensors on the point scale are commonly used. However, these are limited either to one point in space or in time. We present a new, extensive dataset of snow variability in a sub-alpine forest in the Alptal, Switzerland. The core dataset consists of a dense sensor network, repeated high-resolution LiDAR data acquired using a fixed-wing UAV, and manual snow depth and snow density measurements. Using machine learning algorithms, we determine four distinct spatial clusters of similar snow depth dynamics. These clusters are characterized and further used to derive daily snow depth and snow water equivalent (SWE) maps. The results underline the complex relation of topography and canopy cover towards snow accumulation and ablation. The derived products are the first to our knowledge that provide daily, high-resolution snow depth and SWE based almost exclusively on field data. They are therefore ideally suited for the validation of distributed snow models. Our approach can be applied to other project areas and improve our understanding of the spatio-temporal variability of snow in forested environments.

Spatio-temporal Snow Variability in a Sub-Alpine Forest predicted by Machine Learning and UAV-based LiDAR Snow Depth Maps

Joschka Geissler[1], Lars Rathmann[2,3], Markus Weiler[1]

[1]Faculty of Environment and Natural Sciences, Albert-Ludwigs University Freiburg, Friedrichstr.39, 79098 Freiburg, Germany

[2]Department of Sustainable Systems Engineering - INATECH, Albert-Ludwigs-University Freiburg, Emmy-Noether-Str. 2, 79098 Freiburg, Germany

[3]Fraunhofer Institute for Physical Measurement Techniques IPM, Georges-Köhler-Allee 301, Freiburg, Germany

Corresponding author: Joschka Geissler (joschka.geissler@hydrology.uni-freiburg.de)

Key Points:

- A new snow distribution dataset for sub-alpine forests comprising UAV-based LiDAR data, a dense sensor network, and manual measurements.
- A workflow to derive clusters of similar snow dynamics and daily maps of snow water equivalent based exclusively on experimental data.
- The results highlight the importance of forest gap sizes and edges on snow variability.

Abstract

Snow interacts with its environment in many ways, is constantly changing with time, and thus has a highly heterogeneous spatial and temporal variability. Therefore, modeling snow variability is difficult, especially when additional components such as vegetation add complexity. To increase our understanding of the spatio-temporal variability of snow and to validate snow models, we need reliable observation data at similar spatial and temporal scales. For these purposes, airborne LiDAR surveys or time series derived from snow sensors on the point scale are commonly used. However, these are limited either to one point in space or in time. We present a new, extensive dataset of snow variability in a sub-alpine forest in the Alptal, Switzerland. The core dataset consists of a dense sensor network, repeated high-resolution LiDAR data acquired using a fixed-wing UAV, and manual snow depth and snow density measurements. Using machine learning algorithms, we determine four distinct spatial clusters of similar snow depth dynamics. These clusters are characterized and further used to derive daily snow depth and snow water equivalent (SWE) maps. The results underline the complex relation of topography and canopy cover towards snow accumulation and ablation. The derived products are the first to our knowledge that provide daily, high-resolution snow depth and SWE based almost exclusively on field data. They are therefore ideally suited for the validation of distributed snow models. Our approach can be applied to other project areas and improve our understanding of the spatio-temporal variability of snow in forested environments.

Plain Language Summary

Snow distribution, or more precisely the amount of water stored in snow and its spatial variability, depends on the complex interplay of topography, meteorology and vegetation. Scientists try to predict snow distribution as accurately as possible with the help of models. In order to test how well these models represent reality and which processes are relevant to be considered in the models, detailed field measurements are urgently needed. To obtain such data, drones equipped with modern ("LiDAR") sensors are often used to measure the spatial distribution of snow depth, even underneath a tree canopy. In our study, we present a new dataset for an alpine forest in Switzerland. The dataset consists of snow depth maps acquired with a drone, manual measurements and continuous snow depth observations. Based on this dataset, we could show that snow depth in forests and its temporal dynamics reoccur in spatially distinct areas. Furthermore, our approach delivers daily maps of snow depth and snow water equivalent at a spatial resolution of 1 m and can be applied to similar datasets worldwide. Thus, our workflow allows snow models to be tested not only on the days of the drone flight itself, but on a daily basis.

1 Introduction

Water stored in the snowpack plays a crucial role in the hydrologic cycle as it serves as an intermediate storage of winter precipitation and renews groundwater resources (Dozier et al., 2016). It is therefore a prerequisite for functioning eco-hydrologic systems, especially during dry seasons (Siirila-Woodburn et al., 2021; Sturm et al., 2017). Climate change will have various impacts on catchments currently influenced by snow, such as a shift from snow to rain, earlier snowmelt and a decrease in peak snow accumulation (Bormann et al., 2018; López-Moreno et al., 2021; Marty et al., 2017; Notarnicola, 2020). This will reflect on water availability and thus has implications for energy and food production (D. Li et al., 2017). In the European Alps, a continuous seasonal snow cover exists above an elevation of around 1200 m (López-Moreno et al., 2021). As the tree line lies around 2000 m, snow falls on forested and complex topography in a broad altitudinal band. This sub-alpine altitudinal band accounts for 25% of the total area of the European Alps and is thus more widespread in terms of area than the alpine (>2000m altitude) altitudinal band (15%). It is in these sub-alpine environments, that forest and water management strategies are needed to counteract the mentioned climate change impacts and to preserve a functioning eco-hydrologic system (Barnhart et al., 2016; Manning et al., 2022; Niittynen et al., 2018).

Snow cover and its spatio-temporal variability are controlled by vegetation, topography and meteorology (e.g. Mazzotti et al., 2022; Strasser et al., 2011). Assuming low wind speeds, spatial variability of snowfall (accumulation) events over forested areas are dominated by interception and subsequent sublimation processes of snow in the tree canopy. Its magnitude depends strongly on the three-dimensional (3D) structure of the canopy (Moeser et al., 2015; Russell et al., 2021). Interception reduces accumulation in coniferous forests by 30-40%, depending on vegetation characteristics and meteorological conditions (Broxton et al., 2014; Jost et al., 2007; Varhola et al., 2010a). Since vegetation structures are relatively stable, they correlate with the accumulation rates of individual events and, in particular, with the maximum snow distribution at the end of the accumulation period (Koutantou et al., 2022; Mazzotti et al., 2022; Pflug & Lundquist, 2020; Varhola et al., 2010a). Snow melt (ablation) and its spatial variability, however, is much more complex. The prerequisite for ablation, thus water percolation out of the snowpack, is a completely saturated ("ripe") snowpack. The metamorphosis to this state and the subsequent ablation itself, is determined by the sum of the energy inputs to the snow cover. Energy inputs are dominated by longwave (LWR) and shortwave radiation (SWR), latent heat (LH), ground heat and energy from rain. The canopy generally reduces incoming SWR by shading and emits (increases) LWR. However, the magnitude of these effects and thus the change of net energy available for melt depends on the aspect and climate (Mazzotti et al., 2022; Safa et al., 2021), the time during the season (Strasser et al., 2011) and cloud coverage (H.-Y. Li & Wang, 2011). Moreover, if rain falls on snow (RoS), ablation rates can increase and become uncorrelated with the canopy (Garvelmann et al., 2014, 2015).

To adequately predict available water resources in snow-dominated watersheds, snow models are an essential tool for decision-makers, as they can provide spatio-temporal information on the snowpack that cannot be achieved with observations. An encompassing snow model intercomparison study (Essery et al., 2009) concluded that model performance is poor in forested areas, especially for study sites where mean winter air temperatures lie above 0 °C. Since then, much effort has been put into improving hyper-resolution snow models (Gouttevin et al., 2015; Mazzotti et al., 2020b; Mazzotti et al., 2020a). To make use of this gained knowledge in process-level modeling for larger-scale applications, future work should focus on sub-grid model parametrizations (Currier & Lundquist, 2018; Mazzotti et al., 2021). Therefore, a modeling unit (grid-cell) must be explicitly divided into its classes (and their fractions) of similar snow dynamics. For instance, Mazzotti et al. (2022) found classes of similar snow dynamics north of canopy edges, in open terrain and underneath the forest canopy. Schirmer et al. (2011) found repetitive patterns in alpine terrain on lee and windward slopes. Thus, defining such classes is possible but complex and requires study site specific approaches (Currier & Lundquist, 2018). However, promising studies showed that classes of similar snow dynamics, once defined, are transferable to other years (Pflug & Lundquist, 2020; Schirmer et al., 2011).

To measure snow distribution spatially continuously (e.g., for model validation), airborne Light Detection and Ranging (LiDAR) surveys have become the state-of-the-art technology in the field of snow hydrology, as LiDAR can create more robust snow depth maps (HS-maps) compared to other systems and is suitable to measure sub-canopy snow depth (Harder et al., 2020). As commercially available LiDAR sensors are becoming light-weight and affordable, an increasing number of studies have been published using LiDAR-systems mounted on multi-rotor Unmanned Aerial Vehicles (UAV) instead of airplanes (Harder et al., 2020; Jacobs et al., 2021; Koutantou et al., 2022; Rathmann et al., 2021). Compared to LiDAR data acquired using airplanes, UAVs allow reduced revisiting time between surveys (Koutantou et al., 2022), increase point densities and help analyze snow processes at very high spatial resolutions (Russell et al., 2021). The drawback of UAVs is the short flight duration and thus low spatial coverage, making airborne systems still important for larger-scale applications (Kostadinov et al., 2019). A compromise between the high spatial resolution and increased flexibility of UAVs and, on the other side, larger spatial coverages can be achieved using fixed-wing UAVs (Geissler et al., 2021). Fixed-wing UAVs, in contrast to multi-rotor UAVs, are equipped with wings and rely on forward (instead of downward) thrust. Due to limited payload capacities, so far fixed-wing UAVs have only been used in combination with photogrammetric sensors to map snow distribution (Michele et al., 2016).

For the generation of HS-maps from LiDAR, a snow-off and a snow-on survey are needed. From the resulting point clouds, points classified as vegetation are removed. The remaining ground points are typically rasterized to a digital elevation model (DEM) and subtracted from each other. The resulting differential elevation model is then co-registered using snow-free areas such as streets or snow pits to account for systematic vertical shifts between the elevation models. More information on this method can be found in Deems et al. (2013), Koutantou et al. (2022) and Mazzotti et al. (2019). Many of these studies acknowledge that this processing workflow does not consider other than vertical offsets of the original DEMs. However, we are not aware of a study that was able to perform a full co-registration of the snow-on and snow-off surveys comparable to methods used in other fields of research, e.g. for the determination of geodetic glacier mass balances (Nuth & Kääb, 2011).

As remote sensing data is generally limited to a few surveys throughout one season, they are not capable to validate snow model products temporally continuously. Therefore, a spatially continuous validation of hydrologic parameters derived from snow models, such as the season's maximum snow water equivalent (SWE_{max}), ablation and accumulation rates, snow disappearance or fractional snow cover is still difficult to achieve (Mazzotti et al., 2022). Another challenge in creating a non-biased validation dataset is the conversion from the LiDAR-derived HS-maps to SWE-maps, which is typically based on manual or automatic density measurements of the snowpack. However, the interpolation of these density measurements leads to systematic errors of the SWE-maps, especially in mid-winter (Broxton et al., 2019).

In this study, we present a novel dataset consisting of multiple UAV-based LiDAR HS-maps, over a sub-alpine forested study site (0.23 km²) in the European (Pre-)Alps. The LiDAR-derived HS-maps were derived using a fixed-wing UAV. We apply a co-registration approach that considers 3D shifts and rotations between snow-on and snow-off surveys to the HS-maps. The LiDAR-data is supplemented with a dense sensor network of automatic Snow Measuring Stations (SnoMoS) (Varhola et al., 2010b) and repeated manual snow surveys. Besides presenting this comprehensive dataset, the goals of this study are:

(i) To determine and discuss patterns of similar snow dynamics for a sub-alpine forested study site using a clustering workflow.

(ii) To create a spatially and temporally continuous dataset of daily HS- and SWE-maps based only on experimental data.

2 Method

2.1 Study Site and Data

We selected a west-facing hillside of the Alptal, Switzerland (see Figure 1) as study site, which is a sub-alpine catchment that is known for its long history of snow and hydrologic research (Essery et al., 2009; Gouttevin et al., 2015; Stähli et al., 2009; Stähli & Gustafsson, 2006). The forest canopy is heterogeneous with a varying canopy structure and tree heights of up to 35 m. The shape of the project area resulted from the flight planning for the UAV flights, maximizing the surveyed area as well as the aim to minimize snow variability caused by an additional altitude gradient. More details on the study site can be found in Table 1. We collected data throughout a full winter season from 26 November 2021 to 25 April 2022 (Water Year (WY) 2022).

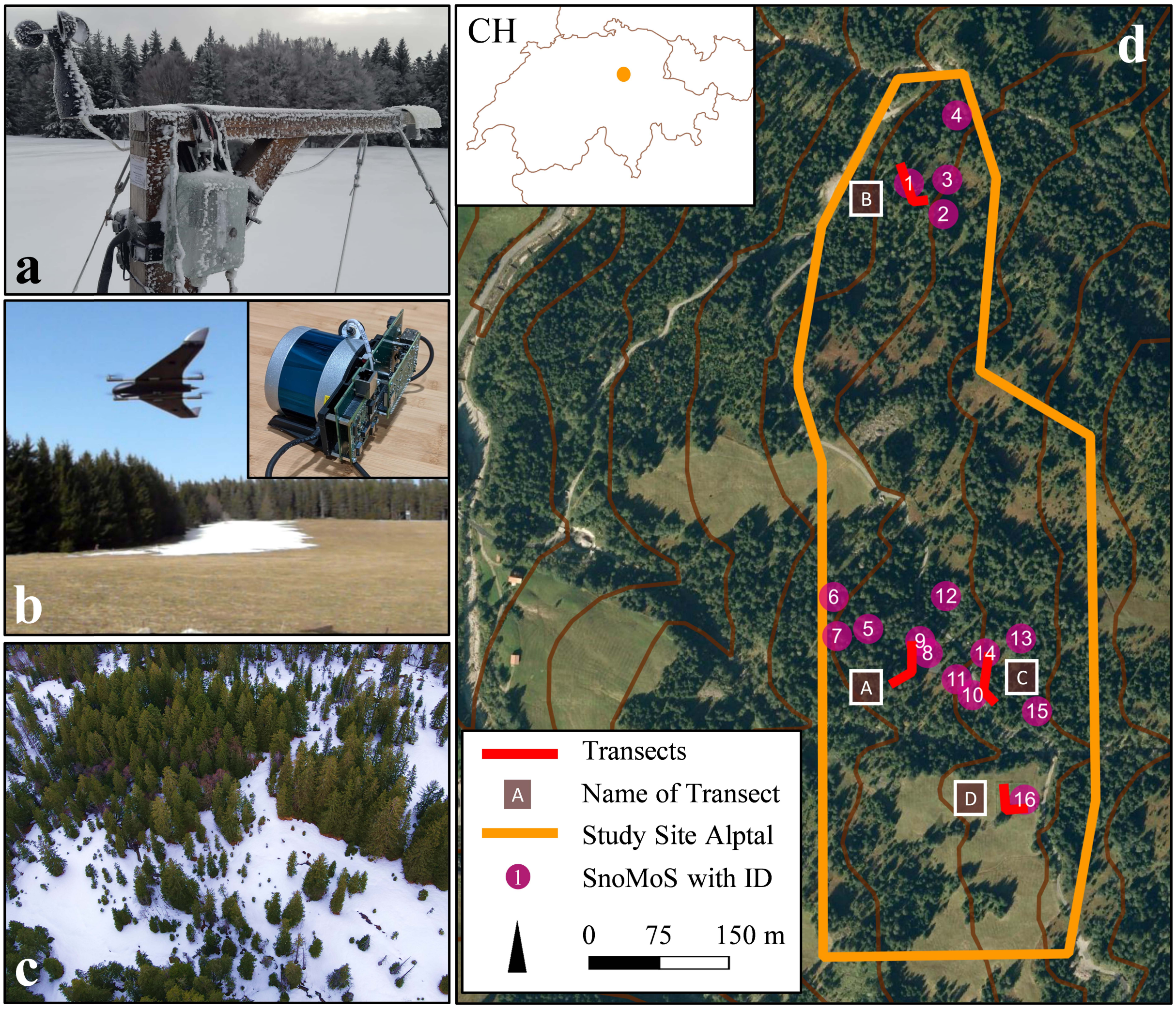

Figure 1: (a) SnoMoS, (b) UAV-based LiDAR system, (c) aerial image of the study site (right: 19 January 2022) and (d) the spatial distribution of the SnoMoS and transects within the study site.

Table 1: Details on our Study Site in the Alptal, Switzerland

Attribute	Value
Coordinates	47°02'33.8"N 8°42'53.3"E
Forest Type	Spruce and Fir
Leaf Area Index	4-5 m²/m²
Maximum Tree Height	35 m
Canopy Coverage	35%
Aspect	West (211° - 296°)
Slope	11° - 25°
Elevation	1170 m – 1240 m
Snow-free Albedo	0.11 (forest) 0.19 (open)
Mean Winter Temperature DJFMA 1989-2019 (WY 2022)	0.5°C; (1.5°C)
Mean Winter Precipitation DJFMA 1989-2019 (WY 2022)	788 mm; (757 mm)

2.1.1. Snow Monitoring Stations

16 SnoMoS (Pohl et al., 2014; Varhola et al., 2010b) (Figure 1-a) were installed to capture the temporal variability of the snowpack at a fixed location with an ultrasonic sensor (MaxBotix MB 7060). The sensors are mounted on wooden bars at around 2 m above ground. Apart from being set on flat terrain with minimal ground vegetation to cover the full spatio-temporal variability of the snowpack, the sensor locations were chosen based on local expert knowledge and information about the canopy (Figure 1-d). SnoMoS 16 is located at the climate station Erlenhoehe, where precipitation and temperature data used in this study (Figure 2) are measured. The sensor configuration was set to measure hourly means and standard deviation (SD) derived from 20 measurements per hour. The raw distance measurements were filtered using thresholds for the SD (< 0.3 m) and the distance (> 0.35 m and < 2.5 m) to eliminate outliers. Snow depth was derived by correcting the raw distance with the data of an internal measuring unit (IMU) and the air temperature. Finally, the corrected height was subtracted from the height of the sensor that was estimated from the sensor measurements right after snow disappearance to minimize the effects of the vegetation. Negative snow depths were set to 0 m and subsequently, the time series were aggregated to daily means. The SnoMoS were equipped with a time-lapse camera to get qualitative information on the snowpack and to fill data gaps (10.2%) using a scale that was painted on the wooden bars. Additionally, snow depth was measured manually at each sensor location after five LiDAR-surveys to estimate the associated error to the SnoMoS snow depth

time series, which resulted in a mean absolute error (MAE) of 2 cm. Figure 2 (bottom) shows the observed daily mean, minimum and maximum snow depth from the SnoMoS.

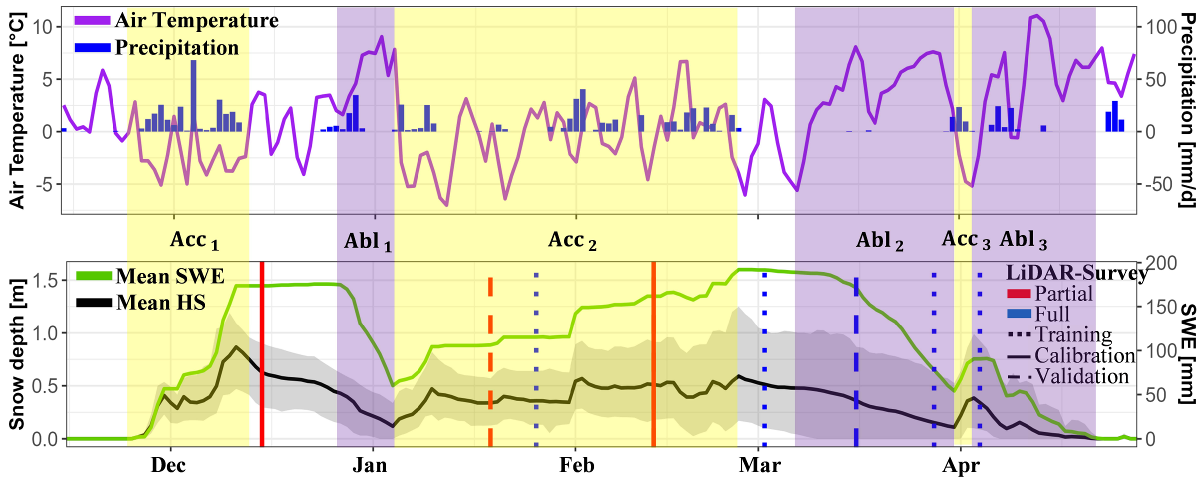

Figure 2: Daily precipitation and air temperature at climate station Erlenhoehe (top); Mean and range of snow depth time series measured by the SnoMoS, mean SWE and dates of LiDAR surveys (bottom); The background color indicates the accumulation (yellow) and ablation (purple) periods.

2.1.2. UAV-based LiDAR

UAV-based LiDAR data was acquired using a customized system comprised by the Velodyne VLP16 Puck Lite multi-beam laser scanner (Dual Return, 905 nm) and an Applanix APX-15 inertial navigation system for direct geo-referencing (Jacobs et al., 2021), mounted on the fixed wing UAV DeltaQuad Pro (Figure 1-b). The UAV performs vertical take-offs and landings (VTOL) in multi-copter mode, whereas the flight itself is performed in fixed-wing mode, thus using only one pusher motor. The DeltaQuad Pro has 1.2 kg payload capacity which was enough to carry all hardware components. With this payload, the UAV flew 37 km in 33 min flight time with one battery load (with around 40% remaining battery charge after landing). Wind speeds during flight were below 5 m/s for all surveys.

Flight planning was conducted with the QGroundControl Software (Version 4.1.4), with parallel trajectories (North-South oriented) with 16 m distance and a mean flight altitude of 80 m above ground. Trajectories were flown alternately in opposite directions at an average flight speed of 19 m/s. One UAV survey consisted of two flights (except for 19 January 2022 with only one flight). Both flights covered the same scene to increase point density and decrease data gaps. In total, eight snow-on surveys were conducted and used within this study, five of which covering the full study site (26 January 2022, 02 March 2022, 16 March 2022, 28 March 2022 and 04 April 2022) and three covering only 72% (13 February 2022), 64% (19 January 2022) and 45% (15 December 2021) of the full study area due to meteorologic or regulatory reasons (Figure 2). The snow-off UAV survey, also consisting of two flights, was conducted on 28 April 2022 shortly after melt out and before the vegetation started growing.

We used the proprietary software POSPac UAV Version 8.3 to compute trajectories and associated positional and rotational errors from the APX-15 data using the correction data of a GNSS reference station placed in the field before each flight campaign. Subsequently, the raw Velodyne data was georeferenced using these trajectories. We associated the respective positioning (i.e. GNSS coordinates) and attitude (i.e. roll, pitch, yaw angles) to each data point additionally. Thereafter, noise was filtered out using the Statistical Outlier Removal algorithm (Rusu & Cousins, 2011) as well as thresholds for the positional and rotational errors using the open-source software CloudCompare (CloudCompare, 2022).

For each UAV survey within the post-processing the pre-processed point cloud of the second flight was co-registered to the complementary point cloud of the same day's first flight. Subsequently, the co-registered point clouds were merged. For the generation of the final LiDAR product, namely the HS-maps, the combined snow-off point cloud was co-registered with the combined snow-on point cloud. Finally, all point clouds were rasterized to a 1 m spatial resolution. We used three 3m x 3m snow pits, distributed within the study area to correct the final HS-maps vertically by the mean within these areas. To exclude further obvious (but rare) outliers, we excluded snow depths below – 0.15 m and above 3 m. Remaining negative values are subsequently set to 0 m.

The co-registrations of two point clouds, as described above, followed four steps: i) the point clouds are cut to the study area, ii) the point clouds are classified in ground and non-ground points using the Cloth Simulation Filter (CSF) algorithm (Zhang et al., 2016), iii) a 4x4 transformation matrix is determined using the Iterative Closest Point (ICP) algorithm (Besl & McKay, 1992; Chen & Medioni, 1992) to co-register non-ground points of the second flights' point cloud (or the combined snow-on) to the first flights point cloud (or the combined snow-off) and finally, iv) the transformation matrix is applied to the full second flight (snow-on) point cloud. This approach accounts for 3D offsets as well as scaling or rotational errors between the point clouds. The post-processing was conducted using the CloudCompare software in command line mode.

Topographic parameters as well as the Canopy Height Model (CHM) of our study site were derived from R (R Core Team, 2021) using the raster (Robert J. Hijmans, 2021) and lidR (Roussel et al., 2020) Package in 1 m spatial resolution. Canopy Cover fraction (CC) (proportion of forested area to total area within a given radius) was derived for a radius of 5 m from the CHM following Mazzotti et al. (2020a).

2.1.3. Snow Survey

The dataset is complemented by manual snow survey data. Within six hours after each LiDAR survey, snow depth (every meter) and SWE (every five meters) were measured along four transects (Figure 1-d) using snow sampling tubes. The transect locations were chosen to capture a high variability of the snow depth within each sub-plot and to be accessible with minimum impact on the snowpack. In line with Neumann et al. (2006), all transects are 50 m long and L-shaped. All LiDAR, HS- and SWE-maps within this study are validated with these measurements.

Snow transects and sensor locations were geolocated using a Leica GNSS system (GS18 and CS20) with accuracies between 0.001 m and 0.35 m depending on the canopy cover.

2.2 Clustering Workflow

We combine the spatial information from the LiDAR-derived HS-maps and the temporal information from the SnoMoS time series to receive daily HS-maps. To achieve this, we apply a workflow based on an unsupervised classification (Figure 3). The workflow is implemented in R, using the packages randomForest (Breiman, 2001), mice (van Buuren & Groothuis-Oudshoorn, 2011), raster and nixmass (Winkler et al., 2021).

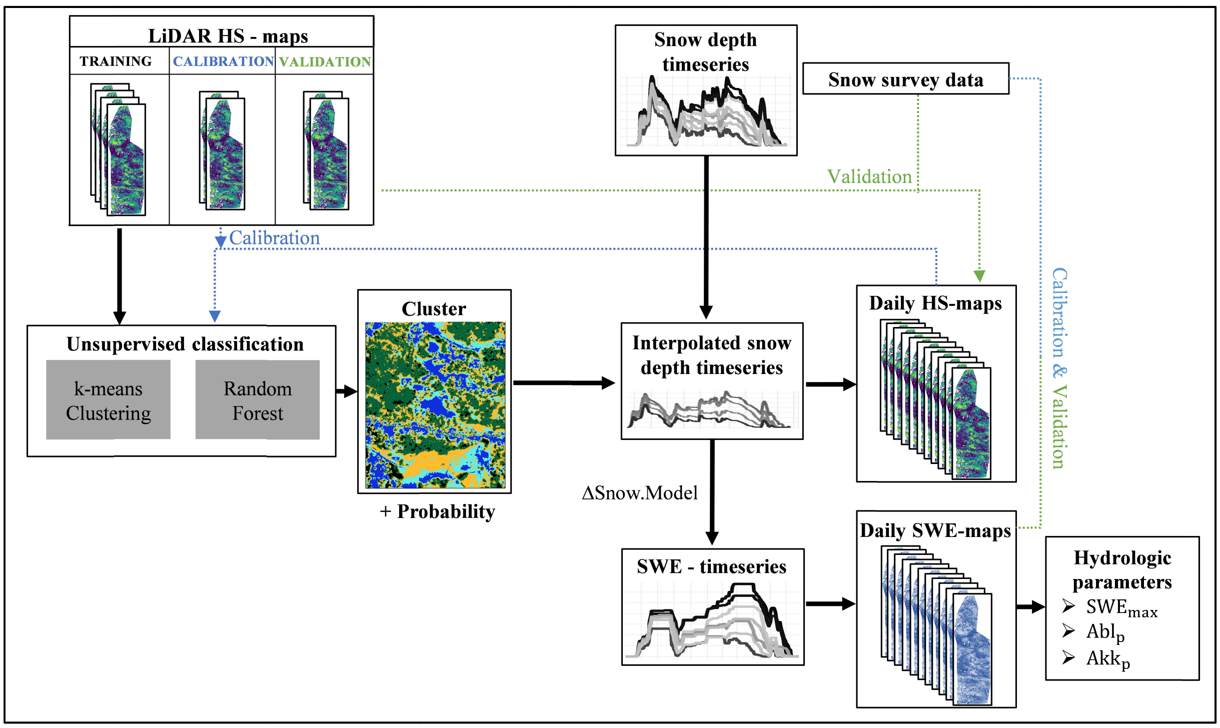

Figure 3: Data Mining Workflow from processed LiDAR HS-maps and snow depth time series to hydrologic output.

As a first step, data gaps within the LiDAR HS-maps are filled using data imputation. Only raster cells that were observed at least five times throughout all eight LiDAR surveys are imputed. This iterative approach fills missing values of the respective cells using the weighted average of the non-missing observations, whereby a proximity matrix to other cells is used as weights. The proximity matrices are derived from a random forest model. For more information on imputing missing values, we refer to van Buuren and Groothuis-Oudshoorn (2011).

The imputed eight LiDAR surveys are subsequently split into four surveys for model training, two surveys for model calibration and two surveys for final model validation (Figure 2, bottom). The model itself consists of a two-step unsupervised classification (clustering): The k-means clustering algorithm (Hartigan & Wong, 1979) first detects clusters in a small subsample of the training data. These detected clusters serve as the target variables within a subsequent random forest classification. As a result, a map is generated for each cluster providing allocation probabilities for each cell to the respective cluster. Next, we combine these clusters with the observed temporal information from the SnoMoS. More precisely, we derive snow depth time series for each cluster c based on the relative probability of the SnoMoS locations belonging to one of the clusters $\mathrm{w_c}$ (Supporting information, S2). Snow depth of a grid cell $\mathrm{HS_{ij}}$ on a day t (daily HS-maps) is then derived by the sum of the probabilities of the respective cell belonging to a cluster c $\mathrm{w_{ij,c}}$ and the snow depth for each cluster on that day (Equation 1).

$$\mathrm{HS_{ij}(t)} = \sum \mathrm{w_{ij,c}} \cdot \left(\frac{\mathrm{w_c}}{\sum \mathrm{w_c}} \cdot \mathrm{HS(t)}\right) \tag{1}$$

For the calibration of the model parameters two independent UAV surveys are used (Figure 2, bottom).The model is then run with parameters on default, changing only one parameter within a given range and step width. Each set of model parameters is run 50 times to derive the mean as well as the variance of the goodness-of-fit metrics. The final value for the model parameters is then derived from the results by minimizing the observed root mean squared error (RMSE) as well as considering computational expense and the interpretability of the results (Supporting information, S1). The final model configuration is then validated using the remaining two UAV surveys (see Figure 2, bottom) as well as snow survey data (See Figure 4).

In this study, the error associated with the derived products is evaluated using the RMSE and MAE as well as the Pearson's correlation coefficient R. We also provide the normalized version of RMSE and MAE (NRMSE and NMAE) for error intercomparisons (normalized by dividing the original error metrics by the mean of the observations).

2.3 SWE-maps and derived products

To derive the hydrologically important SWE, we convert the daily HS-maps to daily SWE-maps. We selected the ΔSnow.Model (Winkler et al., 2021) to process the snow depth time series of the clusters. Daily SWE-maps are then derived following the same method as for the HS-maps (Equation 1). The model is calibrated and subsequently validated against 50% of the available snow survey data respectively to increase model performance. Calibration results can be found in the supporting information, S1.

Snow hydrologic variables are derived from the daily SWE-maps for each raster cell individually: The maximum SWE ($\mathrm{SWE_{max}}$ [mm]), the mean ablation rate ($\mathrm{Abl_p}[\frac{\mathrm{mm}}{\mathrm{d}}]$) and the mean accumulation rate ($\mathrm{Acc_p}[\frac{\mathrm{mm}}{\mathrm{d}}]$). $\mathrm{SWE_{max}}$ is defined by the maximum SWE throughout the whole season, whereas the rates result from the absolute change of SWE for each period (Figure 2) divided by the length of the period in days. For the determination of the $\mathrm{Abl_p}$, only days in which snow was present and absolute rates exceeded 1 mm/d are considered. In the following, the ablation rates are denoted as $\mathrm{Abl_p}$ with p being the number of the period (Figure 2 and Sect. 3.1.). The overall ablation rate derived (summed change of SWE in all periods p divided by the length of all periods p in days) is referred to as the $\mathrm{Abl_{total}}$. The same nomenclature is used for the accumulation rates.

3 Results

3.1 Spatio-temporal Variability

Measured within the study area, at the Erlenhoehe climate station, the winter season of WY 2022 (December 2021 to April 2022) had an average temperature of 1.5 °C, which is 1.0 °C warmer than the average of 1989 through 2019. 757 mm of precipitation was measured during these months, thus 4% less than average. The snow season may be summarized in three accumulation, three ablation and two compaction periods (Figure 2). The first accumulation period ($\mathrm{Acc_1}$), between 26 November 2021 and 12 December 2021, is characterized by varying temperatures between -5 °C and 2 °C and 251 mm (peak 68 mm in one day on 04 December 2021) of total precipitation within 16 days. From 12 December 2021 on, a warm period of 12 days led to a compaction of the snowpack. Slight, mixed precipitation (15 mm) occurred between 24 December 2021 and 27 December 2021. Thereafter, temperatures as well as precipitation amounts increased and caused a three-day RoS-induced ablation of the snowpack (19 mm/d, $\mathrm{Abl_1}$). $\mathrm{Abl_1}$ continued during the following warm period until 04 January 2022. A long accumulation period followed with temperatures varying around freezing temperatures until 26 February 2022 ($\mathrm{Acc_2}$, 318 mm and -0.4 °C). March 2022 was the driest march since 1989 with only 2 mm of precipitation and mean air temperatures of 3 °C until 30 March 2022. In this exceptionally dry March, the snowpack densified until 07 March 2022. Thereafter, the second ablation period ($\mathrm{Abl_2}$) was dominated by high temperatures and clear-sky conditions. Ablation was intensified after 14 March 2022, due to high concentrations of Sahara dust deposited on the snowpack during a small precipitation event (14 March 2022) which induced a lowering of the snow albedo. The following third precipitation period ($\mathrm{Acc_3}$) between 31 March 2022 and 02 April 2022 added 47 mm of precipitation within three days at -2 °C mean air temperature. The snowpack completely vanished during the third ablation period ($\mathrm{Abl_3}$) between 03 April 2022 and 25 April 2022, where high temperatures (5 °C) and (mostly liquid) precipitation (110 mm) caused high ablation rates.

3.2 LiDAR HS-maps

The UAV-based LiDAR setup (Sect. 2.1.) achieved an average point density of 126 points/m² per flight. Since almost all UAV surveys consist of two merged flights, an average point density of 219 points/m² was achieved for all UAV surveys. The point density of points classified as ground lies at 118 points/m² on average for all LiDAR surveys. Derived HS-maps contain 8% data gaps on average. The co-registrations included a 3D shift and rotations around all axes.

None of the transformation matrixes determined by the ICP algorithm applies scaling, although the methodology includes the possibility. The ranges of the absolute shift in x- and y- (horizontal), and z- (vertical) direction are 0.01 m to 0.42 m, 0.01 m to 0.22 m and 0.02 m to 0.53 m respectively. The absolute Euler angles of the rotations around the x-, y- and z-axis are 0 ° to 0.006 °, 0.002 ° to 0.03 ° and 0 ° to 0.0003 ° respectively. The final goodness-of-fit metrics of the LiDAR HS-maps can be found in Table 2. Goodness-of-fit variables are relatively constant between the individual LiDAR surveys, with the RMSE varying between 0.085 m and 0.108 m and R between 0.84 and 0.97. However, since the mean snow depth changed throughout the snow surveys, the normalized error metrics change among the surveys. The co-registration including the ICP algorithm in addition to the snow-free areas improves the goodness-of-fit metrics of all LiDAR HS-maps compared to the exclusive registration using solely snow-free areas (NRMSE –2%, R +0.2). If interception was present during the LiDAR survey, the result of the ICP algorithm is biased in the vertical direction by up to 0.3 m. However, it still improves the LiDAR HS-maps error metrics, as the ICP was followed by a correction with the snow-free areas.

3.3 Modeled daily HS and SWE-maps

Following the workflow shown in Figure 3, we derived daily HS and SWE-maps. An animation can be found in the supplementary material (ds01) of this study. Mean associated errors (Figure 4, Table 2) show generally high correlations when compared to the manual snow survey data (R = 0.95 for HS-maps and R = 0.89 for SWE-maps). Relative errors (regarding snow survey data) increase by 5-6% from the daily HS-maps to the daily SWE-maps, and R decreases by 0.06. Given a mean snow depth at snow survey dates of 0.4 m the absolute RMSE of the HS-maps lies at 8 cm (MEA = 6 cm). Regarding the SWE-maps, the measured mean lies at 132 mm, thus the absolute errors are 35 mm (RMSE) and 26 mm (MEA). Error metrics for the HS-maps are higher when compared to the LiDAR HS-maps.

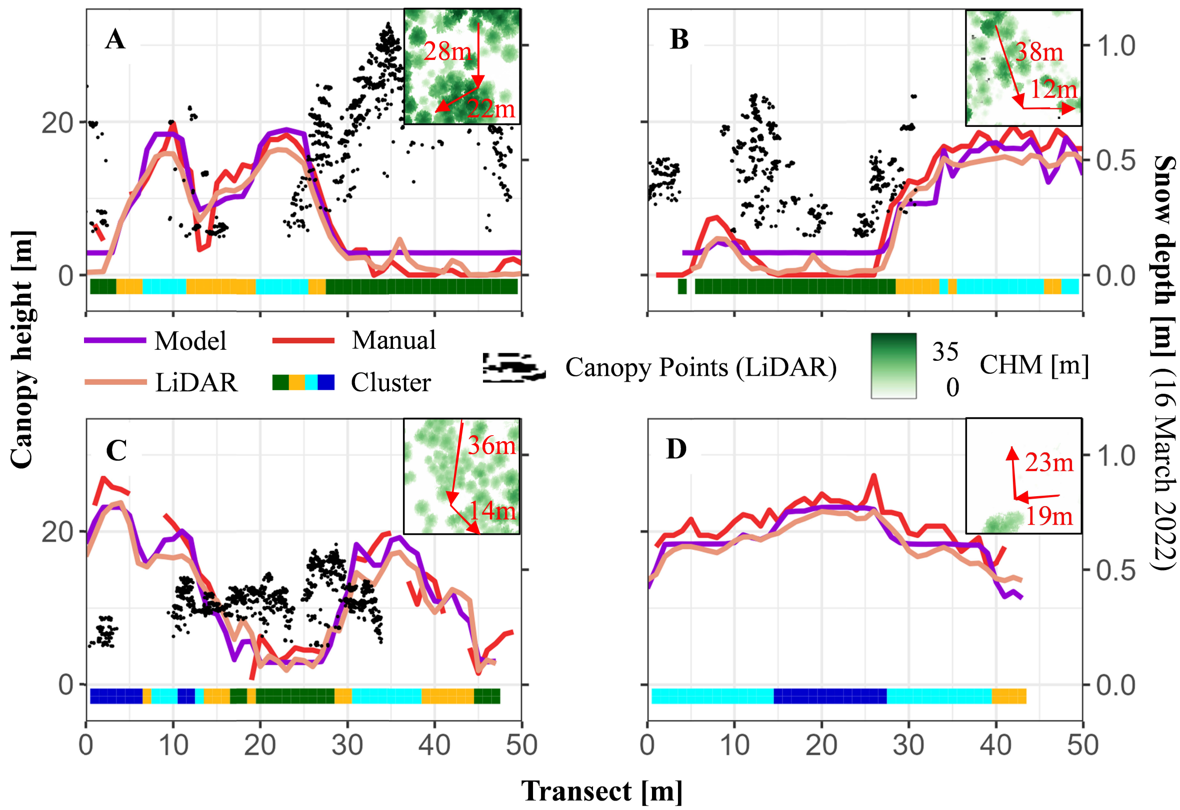

Figure 4: Transects including LiDAR points that were classified as canopy and snow depths derived from manual, LiDAR and daily HS-maps for 16 March 2022. Clusters are shown with their respective color code along the x-axis. An overview of the transect location, direction, canopy height and geometry is given in the small subplots.

Table 2: Error metrics for all derived raster products.

Dataset	Reference	n	NRMSE	NMEA	RMSE	MEA	R
LiDAR HS-maps	Snow Survey	1219	20%	16%	9 cm	7 cm	0.97
HS-maps (modeled)	Snow Survey	348	20%	15%	8 cm	6 cm	0.95
SWE-maps (modeled)	Snow Survey	149	26%	20%	35 mm	26 mm	0.89
HS-maps (modeled)	LiDAR HS-maps	420960	27%	23%	10 cm	7 cm	0.89

3.4 Clusters and derived hydrologic parameters

The methodology presented in section 2.2 resulted in four clusters (Figure 5) of similar snow depth dynamics. The following results combine qualitative (interpretation of clusters relative to canopy) and quantitative analysis (analysis of hydrologic parameters) of the clusters.

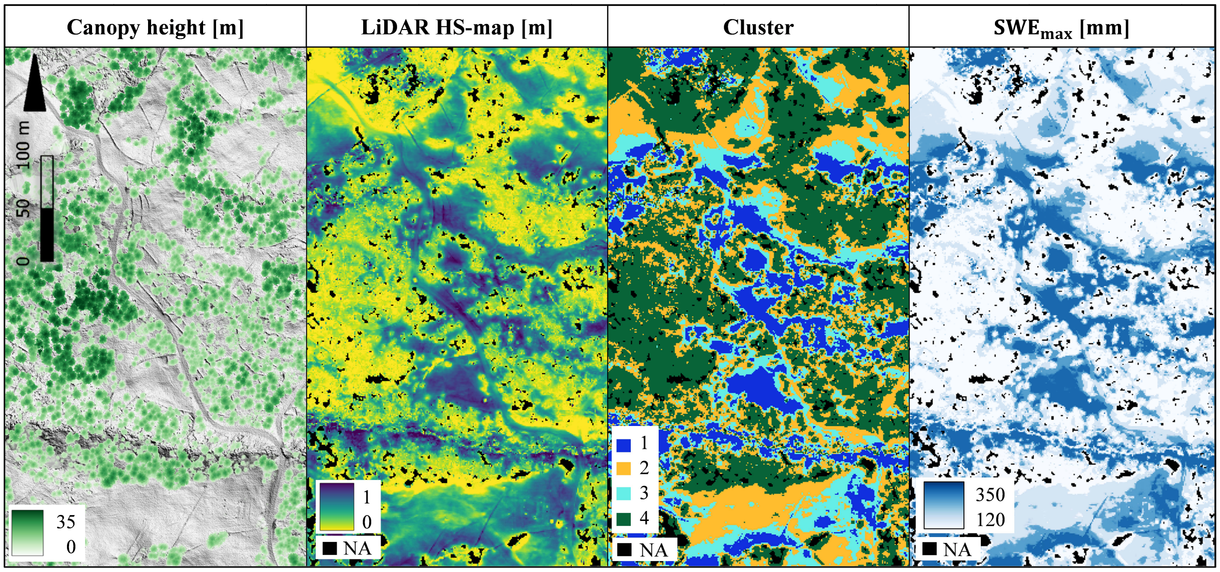

Figure 5: Raster products in 1 m resolution for a subset of our study area. From left to right: Canopy Height Model (CHM) in meters, LiDAR HS-map from 16 March 2022, Cluster with the highest probability, SWE_{max} in mm.

Cluster 1 (in the following referred to as the *open, shaded* cluster) is predominately located in canopy gaps and north of canopy edges in open areas. It has the lowest mean canopy height (0.4 m) and fraction (0.2) compared to the other clusters (Figure 5, Figure 4). Cluster 1 has the highest SWE_{max} of all clusters (305.8 mm). Cluster 2 can be found in open terrain, especially south of canopy edges as well as in small canopy gaps. This cluster is hereafter called *open, exposed*, as it is exposed to either direct SWR (in open terrain) or LWR (in the canopy gaps) (Sect. 4.3). Its SWE_{max} is 136.1 mm and thus lower than cluster 1 and 3. Since cluster 2 can be found in small canopy gaps, mean canopy height (3.8 m) and CC (0.4) increase compared to cluster 1. Intermediate open areas as well as areas that lie on the east/west of canopy edges in open terrain often fall into cluster 3 (*open, intermediate*). Its SWE_{max} (251.5 mm) and canopy metrics (mean canopy height of 1.3 m and CC 0.3) lie in between the *open, shaded* and *open, exposed* cluster. In fact, the spatial arrangement of the clusters 1-3 often corresponds with the order of the respective SWE_{max} (Figure 5). Cluster 4 (*forested*) lies within relatively high (13.5 m) and dense (CC of 0.8) canopy. Its SWE_{max} value (119.3 mm) is the lowest of all clusters. The frequency of occurrence of the clusters ranges from 14% (cluster 1) to 35% (cluster 4). Snow depth and SWE decrease with canopy density throughout the entire season from the *open, shaded* via *open, intermediate* and *open, exposed* to the *forested* cluster (Figure 6 a, b).

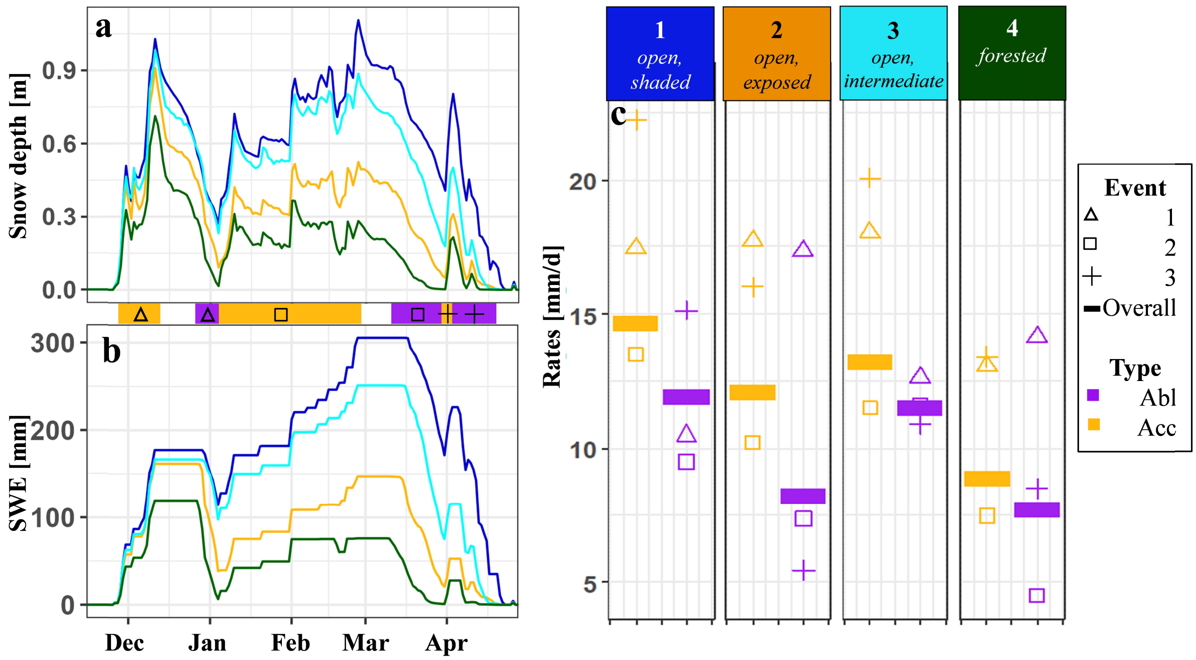

Figure 6: (a) Mean snow depth [m], (b) mean SWE [mm] together with hydrologic periods and (c) absolute accumulation and ablation rates of all clusters.

The overall accumulation rate Acc_{total} is similar for all open clusters but reduced for the forested cluster by 26% to 39% (Figure 6 c). Its correlation to the canopy metrics used is 0.64 (CHM) and 0.62 (CC). The short and heavy snowfall events Acc_1 and Acc_3 show similar dynamics, thus a reduction of the accumulation rate from open to forested areas by 25% to 28% and 16% to 40% respectively. Acc_2 has smaller accumulation rates over a longer period. The accumulation rate of the *forested* cluster is reduced for this period by 27% to 45% compared to the open clusters. However, an imprint of potential radiative differences between the clusters becomes noticeable. Increasing accumulation rates between the three open clusters correspond to the expected decreasing radiation gradient from the *exposed* (10 mm/d) via the *intermediate* (11.5 mm/d) to the *shaded* (13.5 mm/d) cluster (Figure 6). The correlation between the individual accumulation events is high (R: 0.81-0.83).

The overall ablation rate (Abl_{total}) is similar (±0.4 mm/d) for the *open, shaded* and *open, intermediate* clusters. Abl_{total} for the *open, exposed* and *forested* clusters are also similar (± 0.5 mm/d) but reduced by 28% - 36% (Figure 6). Individual ablation events vary strongly in their relative magnitude between clusters. In fact, Abl_1 (mid-winter RoS-event) and Abl_3 (late-winter RoS-event) show opposite relative ablation rate magnitudes in the clusters (R: -0.91): For instance, the *open, exposed* cluster has the highest ablation values (lowest for *open, shaded*) in Abl_1, but lowest (highest) in Abl_3 compared to the other clusters. This is possibly due to different states of the snowpack before the ablation events (Supporting information, S5). During Abl_1, ablation commences in the *forested* cluster (26 December 2022), followed by the *open, exposed* cluster (27 December 2022). Thus, their snowpack is already fully saturated (“ripe“) before the

RoS-event started (28 December to 29 December 2022). Ablation in the remaining two clusters starts with the end of precipitation 29 December 2022 and continues in the following dry period. During Abl_3, snow was only present during the first RoS-event (out of four individual events) for the *open, exposed* and *forested* cluster. Thus, different snow disappearance days during this event influenced the derived mean ablation rate even though we considered this by excluding days where no snow was present in the calculation of these rates (Sect. 2.3). The long and dry ablation period Abl_2 has a weak correlation with the RoS-induced Abl_1 and Abl_3 (R= -0.35 and 0.47). Here, the ablation rates are generally lower compared to the RoS-induced events. During Abl_2, lowest ablation rates can be found in the *forested* cluster and highest in the *open, intermediate* cluster. It is noticeable that ablation start and ablation rate maximum (and its timing) vary between the clusters (Supporting information, S5): for the *forested* cluster, ablation starts on 10 March 2022, followed by the *open, exposed* (14 March 2022), *open, intermediate* (16 March 2022) and *open, shaded* (17 March 2022) clusters. Maximum ablation rates during Abl_2 occur for the *forested* cluster on 16 March 2022 (8.5 mm/d). Compared to the *forested* cluster, ablation rate maxima of the other clusters are higher (maximum of 17.6 mm/d in *open, intermediate*) and later (latest maximum on 27 March 2022 in *open, shaded*).

4 Discussion

4.1 Advantages of presented LiDAR-system and data processing

This study presented the first to our knowledge HS-maps that were derived from a LiDAR sensor mounted on a VTOL fixed-wing UAV. VTOL fixed-wing UAVs allow the start and landing position to be in complex terrain (e.g. canopy gaps with >10 m diameter) and thus eliminate a limitation described in other studies using fixed-wing UAVs (Michele et al., 2016). With a flight duration of more than 60 minutes, the DeltaQuad Pro could cover areas of >1 km² (assuming flat topography). From our experience in winter and complex terrain, the limiting factor was to maintain visual contact with the UAV and a loss of flight stability at wind speeds greater than 5 m/s.

We took advantage of the vegetation information that was measured by the LiDAR during every flight to perform a full (3D) co-registration of i) the point clouds of same-day surveys and ii) the (merged) snow-on and snow-off point clouds. The transformations applied to the point clouds are dominated by a shift in x- and y- (horizontal) and z-direction (vertical). This co-registration, if combined with the final correction of the DEM using the snow-free areas, improved the error metrics of all of our UAV surveys. The result underlines the importance of not limiting the registration to the vertical (z) direction by exclusively using snow-free areas. Shifts in the x- and y- directions can potentially be of the same order of magnitude (for our LiDAR configuration). These observations could describe the observed varying RMSE between different LiDAR acquisitions in other studies (Koutantou et al., 2022). Further testing of this method is needed to test its robustness, for instance against other point densities. For the co-registration, ground control points (reflective tapes of 0.1 m²) were also deployed in the field, as suggested by

Koutantou et al. (2022). However, the derived point densities were not sufficient for a co-registration based on these points.

Accuracies of the presented LiDAR HS-maps (Table 2) have the same order of magnitude compared to other recent studies (Harder et al., 2020; Jacobs et al., 2021; Koutantou et al., 2022). Various sources of error are known from other studies, such as i) snow probes penetrating into the soil (Sturm & Holmgren, 2018), ii) the geolocalisation of reference measurements (Hopkinson et al., 2012), iii) vegetation classified as ground (Jacobs et al., 2021) or iv) errors that result from the LiDAR processing (Deems et al., 2013). We noticed another systematic source of error, caused by the elapsed time between the LiDAR survey (10:00 am to 12:00 pm) and the reference measurements (12:30 pm to 4 pm). This time lag is sufficient for the snowpack to settle, generating an offset between LiDAR and snow survey data. Additionally, a large bias occurred in the LiDAR-derived HS-map where vegetation elements (e.g. fallen tree trunks) were classified as vegetation in the snow-off point cloud and then, when snowed in, were classified as ground in the snow-on point cloud.

We found no differences between forested and open terrain error for this study's LiDAR HS-maps (RMSE of 9 cm and MEA of 8 cm in both terrain types). Jacobs et al. (2021) reported MEA of 1 cm and RMSE of 2 cm for open terrain, and MEA of 7 cm and RMSE of 10 cm for forested terrain using the same LiDAR-system hardware components mounted on a multi-copter UAV. Harder et al. (2020) used different LiDAR-system hardware, also mounted on a multi-rotor UAV. They reported lower error metrics for open terrain (MEA 3-4 cm and RMSE 9-10 cm) but larger errors in forested terrain too (MEA 9-13 cm, RMSE 15-16 cm). More data acquisitions using fixed-wing UAVs are needed to evaluate to what extent error metrics are influenced by this platform's flight characteristics.

4.2 Transferrable workflow for daily HS- and SWE-maps

The proposed workflow (Figure 3) was used to derive clusters with a k-means clustering algorithm followed by a random forest algorithm. We derived daily HS-maps by assigning the temporal information from the snow depth time series, which were measured by the SnoMoS, to the clusters. The derived daily HS-maps are used for the accuracy assessment and thus the calibration and validation of the workflow's parameters.

Since classification algorithms in general can barely handle incomplete data, missing LiDAR observations were imputed in R using the mice package (Doove et al., 2014; Shah et al., 2014). The results allow the application of our workflow to the full project area. Only cells with at least five LiDAR measurements (out of eight surveys) were imputed, which resulted in a total of 14% of the total number of observations that were imputed. Error metrics increased by 0.5 cm (RMSE) and 0.3 cm (MEA) from the original to the imputed LiDAR HS-maps. However, these error estimates must be considered with caution as the number of validation measurements only increased by 10%.

The k-means algorithm is one of the simplest algorithms for unsupervised classification and clustering. Thus, drawbacks that are caused by its simplicity must be taken into account (Ahmed et al., 2020). For instance, the performance of the k-means algorithm is weak for small clusters, data containing outliers or different data types and the result depends on the placement of the initial centroids. However, we chose this algorithm because the training data only contains few outliers and is made up of the same type of data (LiDAR HS-maps) and variable (snow depth in meters). Another disadvantage of the k-means algorithm is that the number of clusters must be specified as a parameter by the user before the clustering. Various methods exist for selecting the number of clusters (Charrad et al., 2014). However, these resulted in a range of recommended number of clusters from two (silhouette width) to five (gap statistic) depending on the selected method. We thus integrated the selection of the number of clusters into the workflow during calibration. However, the selection remains subjective (supporting information, S1). We chose a low number of clusters (despite decreasing RMSE with a higher number of clusters) to increase the interpretability of this study. Note the different maps for model runs with three, four and five clusters in the supporting information, S3. A normalization of the training data was tested but decreased the RMSE of the resulting daily HS-maps by 2 cm. The subsequent random forest algorithm is used to extrapolate clusters found in the subset of the data by the k-means algorithm to the full dataset. The main purpose of the random forest is the generation of a fuzzy (probability-based) result that increased the accuracy of the derived HS-maps compared to a clustering based solely on k-means by 2 cm (RMSE).

SWE is derived from the snow depth time series using the ΔSnow.Model. Technically, no calibration is necessary for this model, as it was calibrated for the European Alps. However, local calibration reduced the NRMSE of the daily SWE-maps by 7% (RMSE changed from 47.6 mm to 37.3 mm) and merely slightly changed the model parameters (see supporting information, S1). Only the k.ov-parameter, a model-specific overburden parameter, changed noticeably (but within the suggested range of Winkler et al. (2021)) and with only low sensitivity. NRMSE increases from the generated HS-maps to the SWE-maps by 6% (Table 2). We suspect that the increased associated error to the SWE-maps is caused by i) the limited capability of ΔSnow.Model to model RoS-events (Winkler et al., 2021), ii) an increased error of the validation data (Beaudoin-Galaise & Jutras, 2022) and iii) a reduced number of validation measurements. However, using the ΔSnow.Model allows us to avoid errors that are otherwise created by the extrapolating of density measurements into space (Broxton et al., 2019).

The derived daily HS- and SWE-maps are not capable of representing extreme values. For instance, a small, south-exposed slope in open terrain (between SnoMoS 2 and 6 (Figure 1) or the north-west corner of Figure 5), falls into the *forested* cluster. In areas as this we find the largest error when comparing the derived HS-maps with the LiDAR-HS-maps. Since such extremes are not covered by the manual snow survey validation data, error metrics of the derived HS-maps increase when compared to the LiDAR data. Future measurement campaigns that want to apply the presented workflow or simply capture the full snow depth variability, are recommended to select SnoMoS locations based on repeated LiDAR data. For our dataset, averaged over all surveys, 11% of the LiDAR HS-map observations had snow depths outside the measured range of the SnoMoS.

The presented workflow is transferrable to different regions and scales. For this study fairly constant topography was imperative to focus on snow distribution patterns driven by canopy cover. However, if the proposed workflow will be used on a study area with more complex terrain (in terms of elevation or aspect) or more profound redistribution of snow due to wind, we expect a larger number of clusters to emerge. For the successful implementation of the presented workflow, SnoMoS must represent the mean of each cluster adequately. Thus, great care must be taken for the choice of adequate locations for point measurements.

4.3 Clusters of snow distribution in forests

The spatial arrangement of the clusters determined by this study's workflow generally divides the study area into *forested* and *open* clusters. The entire sub-canopy variability was aggregated into one cluster. This suggests that under the canopy the snow distribution is relatively constant. In contrast, the *open* clusters are further subdivided, dominantly based on their distance and orientation to the canopy edges, into *exposed, shaded* and *intermediate* clusters. This supports the findings of other studies highlighting the importance of canopy gaps (and their diameter) (Metcalfe & Buttle, 1995, 1998; Seyednasrollah & Kumar, 2014; Sun et al., 2018) as well as distances to canopy edges (Dickerson-Lange et al., 2015; Mazzotti et al., 2019; Mazzotti et al., 2020a). Moreover, the spatial arrangement of the determined clusters corresponds with more conceptual approaches from other studies that were used for defining explicit sub-grid variability for upscaling purposes (Currier et al., 2022; Currier & Lundquist, 2018).

We observed a reduction of the overall accumulation rate between 28% and 36% for the *forested*, compared to the *open* clusters. This observation, dominated by the interception of snow in the canopy, corresponds in its magnitude to existing literature values (Moeser et al., 2015; Russell et al., 2021). The high correlations between individual accumulation events (R: 0.81 – 0.83) also agree with findings by Mazzotti et al. (2022).

Seyednasrollah and Kumar (2014) highlight that ablation rates increase with the gap diameter D relative to the surrounding canopy height H (D/H). This finding was confirmed by this study's clusters: The *open, shaded* clusters are located in canopy gaps of diameters ranging from 12 m to 45 m (D/H 0.4 to 2.1) as well as open terrain that is shaded by canopy. Their overall absolute ablation rate is higher compared to the *open, exposed* cluster, which combines small gaps (D/H <0.5) and open terrain south of canopy edges. In fact, this combination of small canopy gaps and open terrain south of canopy edges within one cluster is counter-intuitive. Small canopy gaps are characterized by reduced SWR (shading) and increased (positive) LWR (radiation emitted by the canopy) whereas open areas are characterized by high SWR (especially in clear-sky conditions) and low (negative) LWR (emitted from the snowpack) (Garvelmann et al., 2014; Strasser et al., 2011). Thus, these areas being combined in one cluster suggests that for our dataset the described effects balance each other out. However, this could limit the transferability of our clusters to other years.

The *open, shaded* cluster often lies spatially adjacent to the *open, intermediate* cluster. The *open, intermediate* cluster differs from the *open, shaded cluster* in slightly lower accumulation rates, (unknown reason), higher ablation rates during the dry and warm march (likely due to less shading) and higher ablation rates during RoS-events, which is potentially due to an earlier saturation of the snowpack.

4.4 Outlook

This study highlights that patterns (“clusters”) of similar snow depth dynamics reoccur in space within forested environments if topography is of minor influence. Further work is needed to evaluate to what extent the observed clusters remain constant among different years. Since Pflug and Lundquist (2020) showed that clusters are inter-annually consistent for years of similar characteristics, this is a promising approach. We expect that the robustness of the observed clusters to inter-annual variability would increase by including LiDAR-derived HS-maps from different seasons in the training data. The presented clusters support conceptual approaches to derive sub-grid variability (Currier & Lundquist, 2018). As they are determined empirically based on LiDAR HS-maps, they could increase our ability to adequately define sub-grid forest variability.

We created daily HS- and SWE-maps by combing these spatial clusters and snow depth time series from multiple point measurements. We see great potential in using the presented dataset for validations of hyper-resolution snow models such as SnowPALM (Broxton et al., 2014), FSM2 (Mazzotti et al., 2020b) or others. This could allow improvements of the respective snow models, entailing the evaluation of mid-winter and late-winter RoS-events.

The presented workflow is transferable to other climates and spatial scales. For many watersheds worldwide LiDAR HS-maps have been acquired in recent years and are often accompanied by point measurements and manual snow survey data. If the presented workflow is applied to these available datasets, daily HS- and SWE-maps can be derived, which are exclusively based on experimental data and data mining algorithms. Moreover, if future work confirms that clusters are inter-annually consistent, this could have positive implications for the availability of experimentally collected data. Clusters, once determined using similar data and the workflow presented, could help to regionalize a small number of targeted point measurements into larger scales. Thus, daily HS- and SWE- maps could be derived with only little effort from only a small number of point measurements. Their accuracy, as shown in our study, could be monitored (if possible) via transects.

This study provided i) a full co-registration workflow of LiDAR point clouds for a more robust generation of HS-maps, ii) a workflow to derive clusters of snow variability, iii) an experimental snow distribution dataset, continuous in space and time and iv) insights into various accumulation and ablation events in forested environments. It thus contributes towards a better process understanding and model representation of forest-snow interaction in the field of snow hydrology. The latter two can help to improve forest and water management strategies that preserve a functioning eco-hydrologic system in a changing climate.

5 Conclusion

This study presents LiDAR HS-maps using a VTOL UAV and underlines its advantages of longer flight durations (compared to multi-rotor UAVs) and the ability to start and land in complex terrain (compared to other fixed-wing UAVs). We perform a full co-registration of the snow-on and snow-off point clouds and thereby obtain constant error metrics for all eight surveys (RMSE between 0.085 m and 0.108 m). Based on the co-registered LiDAR HS-maps, this study determines four clusters of similar snow depth dynamics throughout the winter season of WY 2022 for the forested, sub-alpine study site Alptal in the European Alps (Switzerland). The clusters underline that spatio-temporal variability in forested environments is driven by horizontal and vertical canopy structures (canopy height and gap sizes), considering a neglectable topography. We further derive daily, spatially continuous SWE (and HS) maps based on these clusters. They are exclusively based on experimental data and data mining algorithms and correspond with manual observations (RMSE of SWE-maps: 35 mm and of HS-maps: 9 cm). The presented dataset is thus ideally suited to validate hyper-resolution snow models. The daily SWE-maps and derived hydrologic parameters give detailed insights into individual accumulation and ablation events.

This study's experimental setup and methodology are transferable to other regions, spatial and temporal scales. They can be used to i) create similar snow model validation data sets, ii) determine clusters of similar snow depth dynamics, or iii) evaluate event-based processes spatially continuously within the study site. Such clusters (once determined) can help to decrease the number of point measurements needed to represent the full spatio-temporal variability of a study site. Finally, they can improve the representation of small-scale canopy structure effects on snow distributions in larger-scale models. Further research is needed to evaluate to what extent these clusters repeat inter-annually.

Author contributions

JG and MW designed the study. JG carried out the fieldwork, with support from LR. LR set up the LiDAR system and integrated it into the UAV. LR processed the raw LiDAR data. JG performed the co-registration of the LiDAR data as well as the clustering and subsequent analysis, with input from MW. JG wrote the manuscript, with feedback and support from all authors.

Acknowledgment

The authors thank Jonas Schwarz for his significant support in the fieldwork. We also appreciate the support from Manfred Stähli and Patrick Schleppi who made important contributions for this study. This work would not have been possible without borrowing several SnoMoS from the KIT-Campus Alpine (Benjamin Fersch). Manfred Stähli and Giulia Mazzotti supported the development of the idea for this study and with scientific discussions. I would like to thank Isabel Karst for proofreading and all the support along the way.

Financial support

This study was funded by the German Research Foundation (DFG), project number: 443637229. It is part of the project "*SPENSER: Understanding and Predicting the Spatial and Temporal Variability of Snow Processes Under Different Vegetation Covers Combining Laser Observations and Point Measurements*".

Competing interests

The authors declare that they have no conflict of interest.

Data Availability

The raster data (LiDAR-derived HS-maps, CHM, Digital Terrain Model, Clusters, stacks of daily HS and SWE) used within this study are available at the FreiDok repository from https://doi.org/10.6094/UNIFR/232647 with Creative Commons CC BY-NC-SA license (Geissler et al., 2023). In the same repository, SnoMoS snow depth time series as well as the snow survey data is made available. No registration is required for data download. R-scripts are available from the corresponding author upon request.

6. References

Ahmed, M., Seraj, R., & Islam, S. M. S. (2020). The k-means Algorithm: A Comprehensive Survey and Performance Evaluation. *Electronics*, *9*(8), 1295. https://doi.org/10.3390/electronics9081295

Barnhart, T. B., Molotch, N. P., Livneh, B., Harpold, A. A., Knowles, J. F., & Schneider, D. (2016). Snowmelt rate dictates streamflow. *Geophysical Research Letters*, *43*(15), 8006–8016. https://doi.org/10.1002/2016GL069690

Beaudoin-Galaise, M., & Jutras, S. (2022). Comparison of manual snow water equivalent (SWE) measurements: seeking the reference for a true SWE value in a boreal biome. *The Cryosphere*, *16*(8), 3199–3214. https://doi.org/10.5194/tc-16-3199-2022

Besl, P. J., & McKay, N. D. (1992). A method for registration of 3-D shapes. *IEEE Transactions on Pattern Analysis and Machine Intelligence*, *14*(2), 239–256. https://doi.org/10.1109/34.121791

Bormann, K. J., Brown, R. D., Derksen, C., & Painter, T. H. (2018). Estimating snow-cover trends from space. *Nature Climate Change*, *8*(11), 924–928. https://doi.org/10.1038/s41558-018-0318-3

Breiman, L. (2001). Random forests. *Machine Learning*, *45*(1), 5–32. https://doi.org/10.1023/A:1010933404324

Broxton, P. D., Harpold, A., Biederman, J. A., Troch, P. A., Molotch, N. P., & Brooks, P. D. (2014). Quantifying the effects of vegetation structure on snow accumulation and ablation in mixed-conifer forests. *Ecohydrology*, *8*(6), 1073–1094. https://doi.org/10.1002/eco.1565

Broxton, P. D., Leeuwen, W. J. D., & Biederman, J. A. (2019). Improving Snow Water Equivalent Maps With Machine Learning of Snow Survey and Lidar Measurements. *Water Resources Research*, *55*(5), 3739–3757. https://doi.org/10.1029/2018wr024146

Charrad, M., Ghazzali, N., Boiteau, V., & Niknafs, A. (2014). NbClust : An R Package for Determining the Relevant Number of Clusters in a Data Set. *Journal of Statistical Software*, *61*(6). https://doi.org/10.18637/jss.v061.i06

Chen, Y., & Medioni, G. (1992). Object modelling by registration of multiple range images. *Image and Vision Computing*, *10*(3), 145–155. https://doi.org/10.1016/0262-8856(92)90066-C

CloudCompare. (2022) (Version v2.12.2) [Computer software]. http://www.cloudcompare.org/

Currier, W. R., & Lundquist, J. D. (2018). Snow Depth Variability at the Forest Edge in Multiple Climates in the Western United States. *Water Resources Research*, *54*(11), 8756–8773. https://doi.org/10.1029/2018wr022553

Currier, W. R., Sun, N., Wigmosta, M., Cristea, N., & Lundquist, J. D. (2022). The impact of forest-controlled snow variability on late-season streamflow varies by climatic region and forest structure. *Hydrological Processes*, *36*(6). https://doi.org/10.1002/hyp.14614

Deems, J. S., Painter, T. H., & Finnegan, D. C. (2013). Lidar measurement of snow depth: a review. *Journal of Glaciology*, *59*(215), 467–479. https://doi.org/10.3189/2013JoG12J154

Dickerson-Lange, S. E., Lutz, J. A., Gersonde, R., Martin, K. A., Forsyth, J. E., & Lundquist, J. D. (2015). Observations of distributed snow depth and snow duration within diverse forest structures in a maritime mountain watershed. *Water Resources Research*, *51*(11), 9353–9366. https://doi.org/10.1002/2015wr017873

Doove, L. L., van Buuren, S., & Dusseldorp, E. (2014). Recursive partitioning for missing data imputation in the presence of interaction effects. *Computational Statistics & Data Analysis*, *72*, 92–104. https://doi.org/10.1016/j.csda.2013.10.025

Dozier, J., Bair, E. H., & Davis, R. E. (2016). Estimating the spatial distribution of snow water equivalent in the world's mountains. *WIREs Water*, *3*(3), 461–474. https://doi.org/10.1002/wat2.1140

Essery, R., Rutter, N., Pomeroy, J., Baxter, R., Stähli, M., Gustafsson, D., Barr, A., Bartlett, P., & Elder, K. (2009). SNOWMIP2: An Evaluation of Forest Snow Process Simulations. *Bulletin of the American Meteorological Society*, *90*(8), 1120–1136. https://doi.org/10.1175/2009BAMS2629.1

Garvelmann, J., Pohl, S., & Weiler, M. (2014). Variability of Observed Energy Fluxes during Rain-on-Snow and Clear Sky Snowmelt in a Midlatitude Mountain Environment. *Journal of Hydrometeorology*, *15*(3), 1220–1237. https://doi.org/10.1175/JHM-D-13-0187.1

Garvelmann, J., Pohl, S., & Weiler, M. (2015). Spatio-temporal controls of snowmelt and runoff generation during rain-on-snow events in a mid-latitude mountain catchment. *Hydrological Processes*, *29*(17), 3649–3664. https://doi.org/10.1002/hyp.10460

Geissler, J., Mayer, C., Jubanski, J., Münzer, U., & Siegert, F. (2021). Analyzing glacier retreat and mass balances using aerial and UAV photogrammetry in the Ötztal Alps, Austria. *The Cryosphere*, *15*(8), 3699–3717. https://doi.org/10.5194/tc-15-3699-2021

Geissler, J., Rathmann, L., & Weiler, M. (2023). *Spatio-temporal Snow Variability in the Sub-Alpine Alptal, Switzerland - UAV-based LiDAR Snow Depth Maps and Derived Products* [Research Data]. https://doi.org/10.6094/UNIFR/232647

Gouttevin, I., Lehning, M., Jonas, T., Gustafsson, D., & Mölder, M. (2015). A two-layer canopy model with thermal inertia for an improved snowpack energy balance below needleleaf forest (model SNOWPACK, version 3.2.1, revision 741). *Geoscientific Model Development*, *8*(8), 2379–2398. https://doi.org/10.5194/gmd-8-2379-2015

Harder, P., Pomeroy, J., & Helgason, W. D. (2020). Improving sub-canopy snow depth mapping with unmanned aerial vehicles: Lidar versus structure-from-motion techniques. *The Cryosphere*, *14*(6), 1919–1935. https://doi.org/10.5194/tc-14-1919-2020

Hartigan, J. A., & Wong, M. A. (1979). Algorithm AS 136: A K-Means Clustering Algorithm. *Applied Statistics*, *28*(1), 100. https://doi.org/10.2307/2346830

Hopkinson, C., Pomeroy, J., Debeer, C., Ellis, C. R., & Anderson, A. (2012). Relationships between snowpack depth and primary LiDAR point cloud derivatives in a mountainous environment. *IAHS Publ. 352, 2012*, 354–358.

Jacobs, J. M., Hunsaker, A. G., Sullivan, F. B., Palace, M., Burakowski, E. A., Herrick, C., & Cho, E. (2021). Snow depth mapping with unpiloted aerial system lidar observations: a case study in Durham, New Hampshire, United States. *The Cryosphere*, *15*(3), 1485–1500. https://doi.org/10.5194/tc-15-1485-2021

Jost, G., Weiler, M., Gluns, D. R., & Alila, Y. (2007). The influence of forest and topography on snow accumulation and melt at the watershed-scale. *Journal of Hydrology*, *347*(1-2), 101–115. https://doi.org/10.1016/j.jhydrol.2007.09.006

Kostadinov, T. S., Schumer, R., Hausner, M., Bormann, K. J., Gaffney, R., McGwire, K., Painter, T. H., Tyler, S., & Harpold, A. A. (2019). Watershed-scale mapping of fractional snow cover under conifer forest canopy using lidar. *Remote Sensing of Environment*, *222*, 34–49. https://doi.org/10.1016/j.rse.2018.11.037

Koutantou, K., Mazzotti, G., Brunner, P., Webster, C., & Jonas, T. (2022). Exploring snow distribution dynamics in steep forested slopes with UAV-borne LiDAR. *Cold Regions Science and Technology*, *200*(5), 103587. https://doi.org/10.1016/j.coldregions.2022.103587

Li, D., Wrzesien, M. L., Durand, M., Adam, J., & Lettenmaier, D. P. (2017). How much runoff originates as snow in the western United States, and how will that change in the future? *Geophysical Research Letters*, *44*(12), 6163–6172. https://doi.org/10.1002/2017GL073551

Li, H.-Y., & Wang, J. (2011). Simulation of snow distribution and melt under cloudy conditions in an Alpine watershed. *Hydrology and Earth System Sciences*, *15*(7), 2195–2203. https://doi.org/10.5194/hess-15-2195-2011

López-Moreno, J. I., Pomeroy, J., Morán-Tejeda, E., Revuelto, J., Navarro-Serrano, F. M., Vidaller, I., & Alonso-González, E. (2021). Changes in the frequency of global high mountain rain-on-snow events due to climate warming. *Environmental Research Letters*, *16*(9), 94021. https://doi.org/10.1088/1748-9326/ac0dde

Manning, A. L., Harpold, A., & Csank, A. (2022). Spruce Beetle Outbreak Increases Streamflow From Snow-Dominated Basins in Southwest Colorado, USA. *Water Resources Research*, *58*(5). https://doi.org/10.1029/2021WR029964

Marty, C., Tilg, A.-M., & Jonas, T. (2017). Recent Evidence of Large-Scale Receding Snow Water Equivalents in the European Alps. *Journal of Hydrometeorology*, *18*(4), 1021–1031. https://doi.org/10.1175/jhm-d-16-0188.1

Mazzotti, G., Currier, W. R., Deems, J. S., Pflug, J. M., Lundquist, J. D., & Jonas, T. (2019). Revisiting Snow Cover Variability and Canopy Structure Within Forest Stands: Insights From Airborne Lidar Data. *Water Resources Research*, *55*(7), 6198–6216. https://doi.org/10.1029/2019WR024898

Mazzotti, G., Essery, R., Moeser, C. D., & Jonas, T. (2020a). Resolving Small-Scale Forest Snow Patterns Using an Energy Balance Snow Model With a One-Layer Canopy. *Water Resources Research*, *56*(1). https://doi.org/10.1029/2019WR026129

Mazzotti, G., Essery, R., Webster, C., Malle, J., & Jonas, T. (2020b). Process-Level Evaluation of a Hyper-Resolution Forest Snow Model Using Distributed Multisensor Observations. *Water Resources Research*, *56*(9). https://doi.org/10.1029/2020WR027572

Mazzotti, G., Webster, C., Essery, R., & Jonas, T. (2021). Increasing the Physical Representation of Forest-Snow Processes in Coarse-Resolution Models: Lessons Learned From Upscaling Hyper-Resolution Simulations. *Water Resources Research*, *57*(5). https://doi.org/10.1029/2020WR029064

Mazzotti, G., Webster, C., Quéno, L., Cluzet, B., & Jonas, T. (2022). Canopy structure, topography and weather are equally important drivers of small-scale snow cover dynamics in sub-alpine forests. *Hydrology and Earth System Sciences Discussions*, *2022*, 1–32. https://doi.org/10.5194/hess-2022-273

Metcalfe, R. A., & Buttle, J. M. (1995). Controls of Canopy Structure on Snowmelt Rates in the Boreal Forest. In *Proceedings of the Annual Eastern Snow Conference.* Symposium conducted at the meeting of Eastern Snow Conference.

Metcalfe, R. A., & Buttle, J. M. (1998). A statistical model of spatially distributed snowmelt rates in a boreal forest basin. *Hydrological Processes*, *12*(10-11), 1701–1722. https://doi.org/10.1002/(sici)1099-1085(199808/09)12:10/11<1701::aid-hyp690>3.0.co;2-d

Michele, C. de, Avanzi, F., Passoni, D., Barzaghi, R., Pinto, L., Dosso, P., Ghezzi, A., Gianatti, R., & Della Vedova, G. (2016). Using a fixed-wing UAS to map snow depth distribution: an evaluation at peak accumulation. *The Cryosphere*, *10*(2), 511–522. https://doi.org/10.5194/tc-10-511-2016

Moeser, D., Stähli, M., & Jonas, T. (2015). Improved snow interception modeling using canopy parameters derived from airborne L i DAR data. *Water Resources Research*, *51*(7), 5041–5059. https://doi.org/10.1002/2014wr016724

Neumann, N. N., Derksen, C., Smith, C., & Goodison, B. (2006). Characterizing local scale snow cover using point measurements during the winter season. *Atmosphere-Ocean*, *44*(3), 257–269. https://doi.org/10.3137/ao.440304

Niittynen, P., Heikkinen, R. K., & Luoto, M. (2018). Snow cover is a neglected driver of Arctic biodiversity loss. *Nature Climate Change*, *8*(11), 997–1001. https://doi.org/10.1038/s41558-018-0311-x

Notarnicola, C. (2020). Hotspots of snow cover changes in global mountain regions over 2000–2018. *Remote Sensing of Environment*, *243*, 111781. https://doi.org/10.1016/j.rse.2020.111781

Nuth, C., & Kääb, A. (2011). Co-registration and bias corrections of satellite elevation data sets for quantifying glacier thickness change. *The Cryosphere*, *5*(1), 271–290. https://doi.org/10.5194/tc-5-271-2011

Pflug, J. M., & Lundquist, J. D. (2020). Inferring Distributed Snow Depth by Leveraging Snow Pattern Repeatability: Investigation Using 47 Lidar Observations in the Tuolumne Watershed, Sierra Nevada, California. *Water Resources Research*, *56*(9). https://doi.org/10.1029/2020WR027243

Pohl, S., Garvelmann, J., Wawerla, J., & Weiler, M. (2014). Potential of a low-cost sensor network to understand the spatial and temporal dynamics of a mountain snow cover. *Water Resources Research*, *50*(3), 2533–2550. https://doi.org/10.1002/2013WR014594

R Core Team. (2021). *R* (Version 4.1.0) [Computer software]. Vienna, Austria. https://www.R-project.org/

Rathmann, L., Geissler, J., & Reiterer, A. (2021). Concept for a novel airborne LiDAR system combining high-resolution snow height mapping with co-registered spatial information on the water content of the snowpack. In E. Stella (Ed.), *Proceedings of SPIE: volume 11785, Multimodal Sensing and Artificial Intelligence: Technologies and Applications II: 21-25 June 2021, online only, Germany* (p. 37). SPIE. https://doi.org/10.1117/12.2591815

Robert J. Hijmans. (2021). *raster: Geographic Data Analysis and Modeling*. https://CRAN.R-project.org/package=raster

Roussel, J.-R., Auty, D., Coops, N. C., Tompalski, P., Goodbody, T. R., Meador, A. S., Bourdon, J.-F., Boissieu, F. de, & Achim, A. (2020). lidR: An R package for analysis of Airborne Laser Scanning (ALS) data. *Remote Sensing of Environment*, *251*, 112061. https://doi.org/10.1016/j.rse.2020.112061

Russell, M., Eitel, J. U. H., Link, T. E., & Silva, C. A. (2021). Important Airborne Lidar Metrics of Canopy Structure for Estimating Snow Interception. *Remote Sensing*, *13*(20), 4188. https://doi.org/10.3390/rs13204188

Rusu, R. B., & Cousins, S. (2011). 3D is here: Point Cloud Library (PCL). *IEEE International Conference on Robotics and Automation*, 1–4. https://doi.org/10.1109/ICRA.2011.5980567

Safa, H., Krogh, S. A., Greenberg, J., Kostadinov, T. S., & Harpold, A. A. (2021). Unraveling the Controls on Snow Disappearance in Montane Conifer Forests Using Multi-Site Lidar. *Water Resources Research*, *57*(12). https://doi.org/10.1029/2020WR027522

Schirmer, M., Wirz, V., Clifton, A., & Lehning, M. (2011). Persistence in intra-annual snow depth distribution: 1. Measurements and topographic control. *Water Resources Research*, *47*(9). https://doi.org/10.1029/2010WR009426

Seyednasrollah, B., & Kumar, M. (2014). Net radiation in a snow-covered discontinuous forest gap for a range of gap sizes and topographic configurations. *Journal of Geophysical Research: Atmospheres*, *119*(17), 10,323-10,342. https://doi.org/10.1002/2014JD021809

Shah, A. D., Bartlett, J. W., Carpenter, J., Nicholas, O., & Hemingway, H. (2014). Comparison of random forest and parametric imputation models for imputing missing data using MICE: A CALIBER study. *American Journal of Epidemiology*, *179*(6), 764–774. https://doi.org/10.1093/aje/kwt312

Siirila-Woodburn, E. R., Rhoades, A. M., Hatchett, B. J., Huning, L. S., Szinai, J., Tague, C., Nico, P. S., Feldman, D. R., Jones, A. D., Collins, W. D., & Kaatz, L. (2021). A low-to-no snow future and its impacts on water resources in the western United States. *Nature Reviews Earth & Environment*, *2*(11), 800–819. https://doi.org/10.1038/s43017-021-00219-y

Stähli, M., & Gustafsson, D. (2006). Long-term investigations of the snow cover in a subalpine semi-forested catchment. *Hydrological Processes*, *20*(2), 411–428. https://doi.org/10.1002/hyp.6058

Stähli, M., Jonas, T., & Gustafsson, D. (2009). The role of snow interception in winter-time radiation processes of a coniferous sub-alpine forest. *Hydrological Processes*, *23*(17), 2498–2512. https://doi.org/10.1002/hyp.7180

Strasser, U., Warscher, M., & Liston, G. E. (2011). Modeling Snow–Canopy Processes on an Idealized Mountain. *Journal of Hydrometeorology*, *12*(4), 663–677. https://doi.org/10.1175/2011JHM1344.1

Sturm, M., Goldstein, M. A., & Parr, C. (2017). Water and life from snow: A trillion dollar science question. *Water Resources Research*, *53*(5), 3534–3544. https://doi.org/10.1002/2017WR020840

Sturm, M., & Holmgren, J. (2018). An Automatic Snow Depth Probe for Field Validation Campaigns. *Water Resources Research*, *54*(11), 9695–9701. https://doi.org/10.1029/2018wr023559

Sun, N., Wigmosta, M., Zhou, T., Lundquist, J. D., Dickerson-Lange, S., & Cristea, N. (2018). Evaluating the functionality and streamflow impacts of explicitly modelling forest-snow interactions and canopy gaps in a distributed hydrologic model. *Hydrological Processes*, *32*(13), 2128–2140. https://doi.org/10.1002/hyp.13150

van Buuren, S., & Groothuis-Oudshoorn, K. (2011). mice : Multivariate Imputation by Chained Equations in R. *Journal of Statistical Software*, *45*(3). https://doi.org/10.18637/jss.v045.i03

Varhola, A., Coops, N. C., Weiler, M., & Moore, R. D. (2010a). Forest canopy effects on snow accumulation and ablation: An integrative review of empirical results. *Journal of Hydrology*, *392*(3-4), 219–233. https://doi.org/10.1016/j.jhydrol.2010.08.009

Varhola, A., Wawerla, J., Weiler, M., Coops, N. C., Bewley, D., & Alila, Y. (2010b). A New Low-Cost, Stand-Alone Sensor System for Snow Monitoring. *Journal of Atmospheric* *and Oceanic Technology*, *27*(12), 1973–1978. https://doi.org/10.1175/2010JTECHA1508.1

Winkler, M., Schellander, H., & Gruber, S. (2021). Snow water equivalents exclusively from snow depths and their temporal changes: the Δsnow model. *Hydrology and Earth System Sciences*, *25*(3), 1165–1187. https://doi.org/10.5194/hess-25-1165-2021

Zhang, W., Qi, J., Wan, P., Wang, H., Xie, D., Wang, X., & Yan, G. (2016). An Easy-to-Use Airborne LiDAR Data Filtering Method Based on Cloth Simulation. *Remote Sensing*, *8*(6), 501. https://doi.org/10.3390/rs8060501

Water Resources Research

Supporting Information for

Spatio-temporal Snow Variability in a Sub-Alpine Forest predicted by Machine Learning and UAV-based LiDAR Snow Depth Maps

Joschka Geissler[1], Lars Rathmann[2,3], Markus Weiler[1]

[1]Faculty of Environment and Natural Sciences, Albert-Ludwigs University Freiburg, Friedrichstr.39, 79098 Freiburg, Germany

[2]Department of Sustainable Systems Engineering - INATECH, Albert-Ludwigs-University Freiburg, Emmy-Noether-Str. 2, 79098 Freiburg, Germany

[3]Fraunhofer Institute for Physical Measurement Techniques IPM, Georges-Köhler-Allee 301, Freiburg, Germany

Contents of this file

Figures S1 to S6

Additional Supporting Information (Files uploaded separately)

Captions for Movie S1

Introduction

The supporting information contains six figures and one movie that should give the interested reader background information on the presented workflow and data set. S1 contains the results of the calibration, where the strongly varying sensitivity of the individual parameters becomes clear. Building on this, S2 visualizes the probability based contributions of the individual SnoMoS to the time series of the clusters (c.f. Equation 1 of the main publication). S3 shows how the clusters change depending on the pre-defined number-of-clusters (‘*nclass*’*)* parameter. S4 and S5 can be used by the interested reader for a more in-depth analysis of the accumulation and ablation dynamics during the individual events. The density information included in these figures is based solely on the quotient of maximum snow water equivalent (SWE) - and snow depth (HS)- maps and must therefore be considered with caution. Finally, S6 provides the spatial distribution of the clusters, the maximum SWE and canopy height model (CHM) for the entire study site for the sake of completeness (compare with sub-plots of Figure 5). An animation of the daily SWE-maps is uploaded separately as ds01.

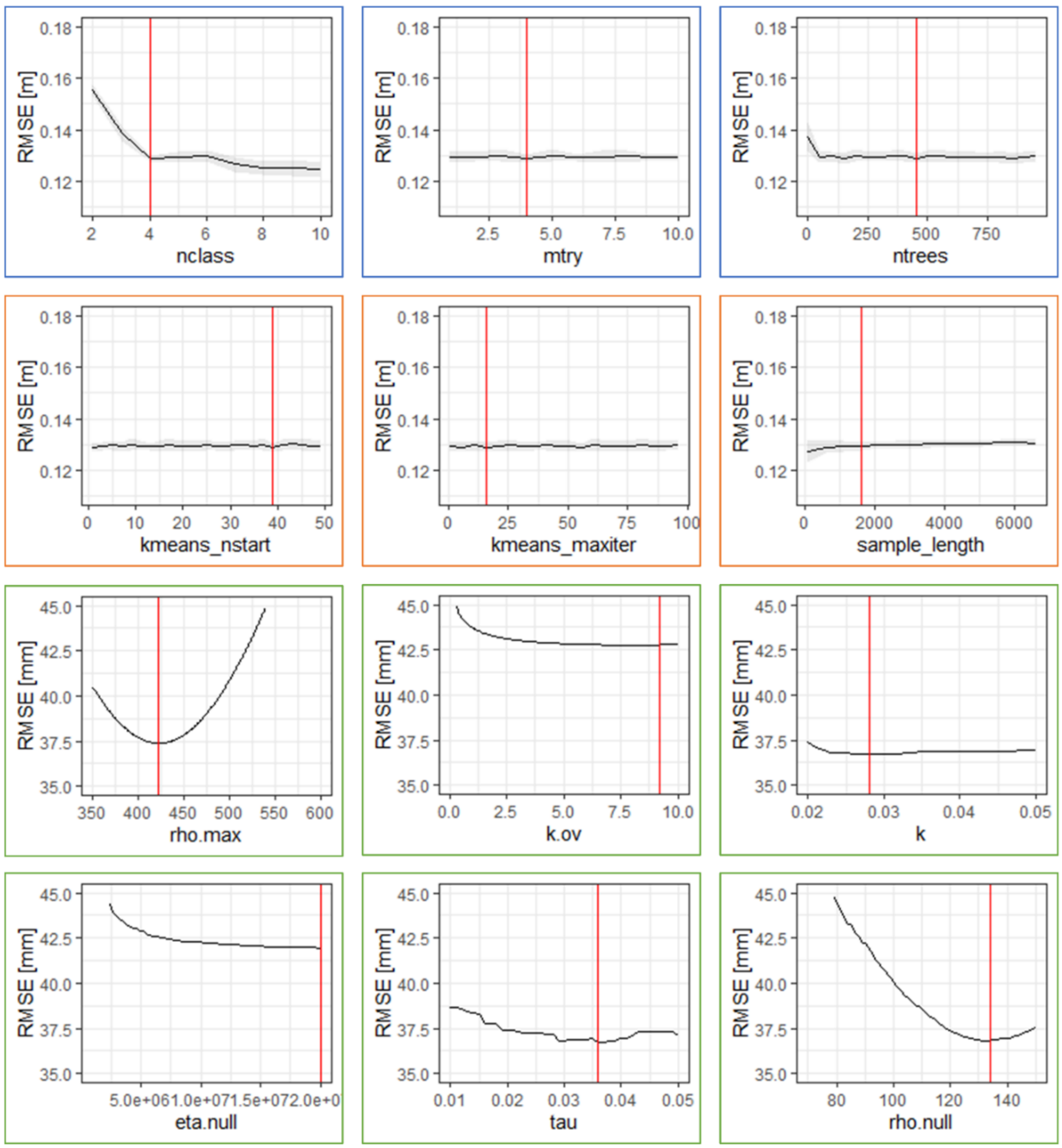

Figure S1. Calibration result of the unsupervised classification model and of the ΔSnow.Model; Blue boxes are hyperparameters from the random forest model, orange are from the k-means–algorithm and green from the ΔSnow.Model; Black lines show the mean RMSE, grey ranges indicate the standard deviation of 50 model runs for the respective parameter value. The final value chosen is illustrated by the vertical red line.

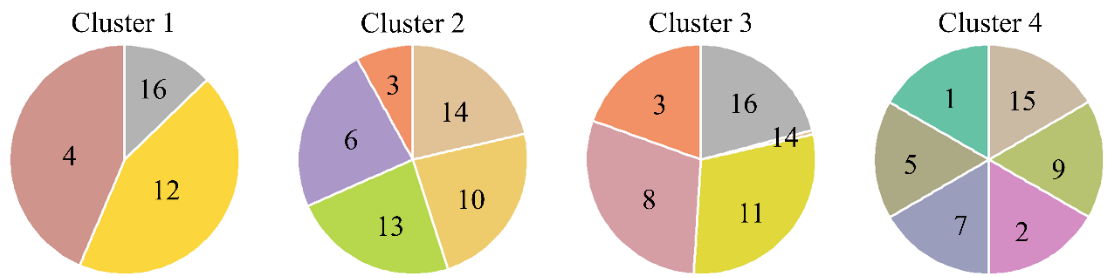

Figure S2. Probability based contributions of the individual SnoMoS time series to the time series of the Clusters (Equation 1). (Locations of the SnoMoS can be found in the main publication, Figure 1)

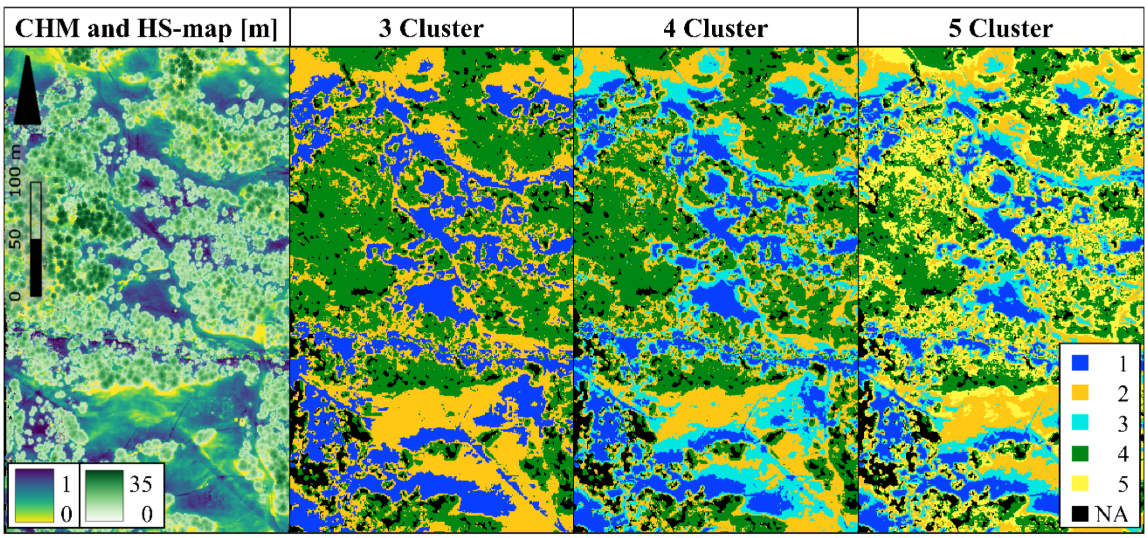

Figure S3. CHM and HS-map (16 March 2022) of a sub-area of the study site (left) and different numbers of clusters determined with the workflow presented in the main publication. Resolution of the raster data is 1 m.

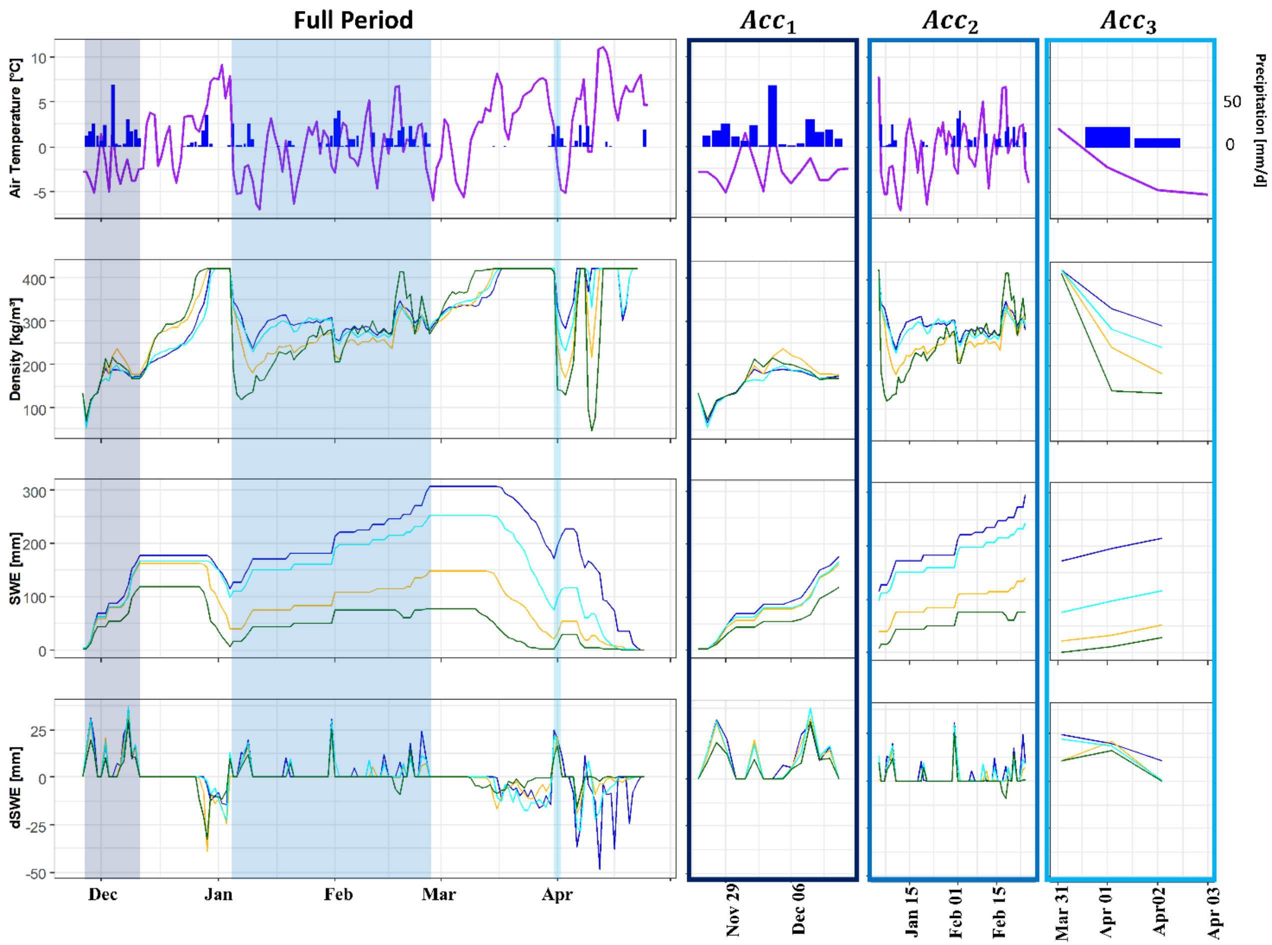

Figure S4. Time series of daily temperature and precipitation at climate station Erlenhoehe, mean daily density (derived by dividing daily SWE-maps by daily HS-maps) in kg/m³, SWE in mm and daily change of SWE in mm for the individual clusters over the entire season as well as the individual accumulation events.

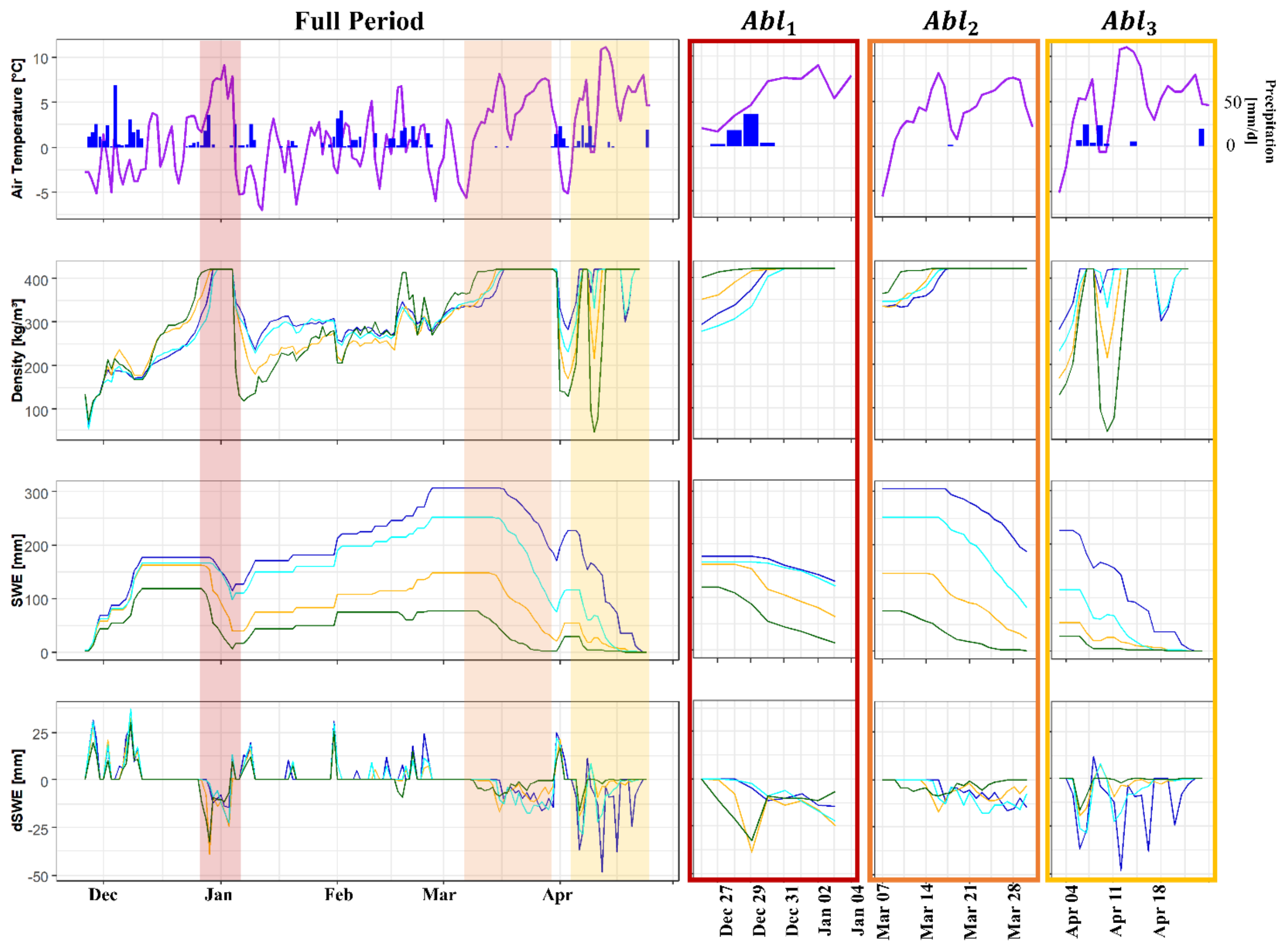

Figure S5. Time series of daily temperature and precipitation at climate station Erlenhoehe, mean daily Density (derived by dividing daily SWE-maps by daily HS-maps) in kg/m^3, SWE in mm and daily change of SWE in mm for the individual clusters over the entire season as well as the individual ablation events.

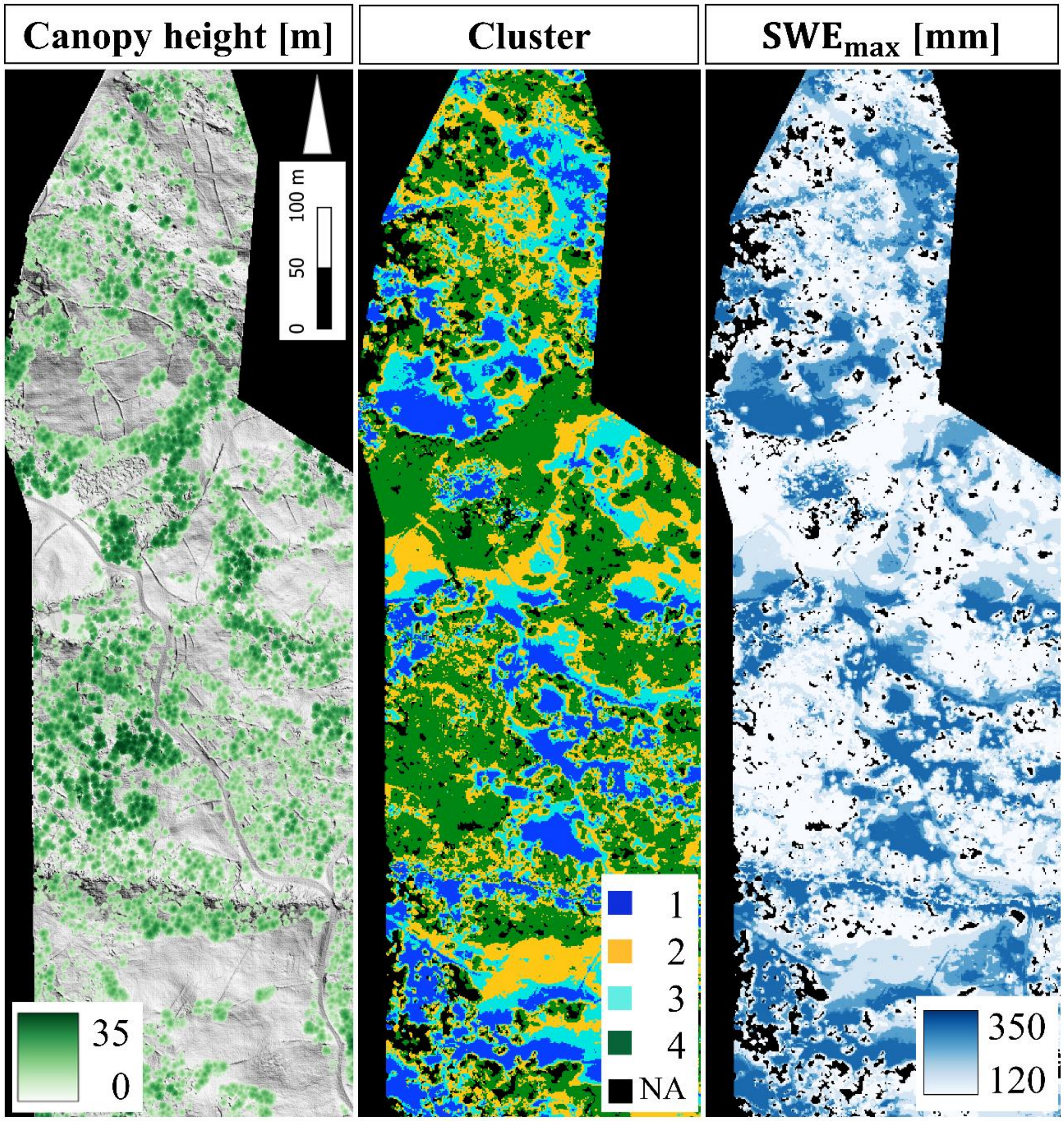

Figure S6. Canopy Height Model, map of Clusters and maximum SWE for the entire study area in 1 m spatial resolution.

Data Set DS1. Animation of daily SWE maps in mm and 1 m spatial resolution.